J. Fluid Mech. (1989), *vol.* 206, *pp.* 75–104
Printed in Great Britain

Three-dimensional thermal convection in a spherical shell

By D. BERCOVICI,[1] G. SCHUBERT,[1] G. A. GLATZMAIER[2] AND A. ZEBIB[3]

[1] Department of Earth and Space Sciences, University of California, Los Angeles, CA 90024, USA

[2] Earth and Space Sciences Division, Los Alamos National Laboratory, Los Alamos, NM 87545, USA

[3] Department of Mechanical and Aerospace Engineering, Rutgers University, New Brunswick, NJ 08903, USA

(Received 7 December 1987 and in revised form 16 February 1989)

Independent pseudo-spectral and Galerkin numerical codes are used to investigate three-dimensional infinite Prandtl number thermal convection of a Boussinesq fluid in a spherical shell with constant gravity and an inner to outer radius ratio equal to 0.55. The shell is heated entirely from below and has isothermal, stress-free boundaries. Nonlinear solutions are validated by comparing results from the two codes for an axisymmetric solution at Rayleigh number $Ra = 14250$ and three fully three-dimensional solutions at $Ra = 2000$, 3500 and 7000 (the onset of convection occurs at $Ra = 712$). In addition, the solutions are compared with the predictions of a slightly nonlinear analytic theory. The axisymmetric solution is equatorially symmetric and has two convection cells with upwelling at the poles. Two dominant planforms of convection exist for the three-dimensional solutions: a cubic pattern with six upwelling cylindrical plumes, and a tetrahedral pattern with four upwelling plumes. The cubic and tetrahedral patterns persist for Ra at least up to 70000. Time dependence does not occur for these solutions for $Ra \leqslant 70000$, although for $Ra > 35000$ the solutions have a slow asymptotic approach to steady state. The horizontal and vertical structure of the velocity and temperature fields, and the global and three-dimensional heat flow characteristics of the various solutions are investigated for the two patterns up to $Ra = 70000$. For both patterns at all Ra, the maximum velocity and temperature anomalies are greater in the upwelling regions than in the downwelling ones and heat flow through the upwelling regions is almost an order of magnitude greater than the mean heat flow. The preferred mode of upwelling is cylindrical plumes which change their basic shape with depth. Downwelling occurs in the form of connected two-dimensional sheets that break up into a network of broad plumes in the lower part of the spherical shell. Finally, the stability of the two patterns to reversal of flow direction is tested and it is found that reversed solutions exist only for the tetrahedral pattern at low Ra.

1. Introduction

The study of thermal convection in highly viscous (i.e. infinite Prandtl number, Pr) spherical fluid shells is important for its application to the structure and evolution of the terrestrial planets (Schubert, Stevenson & Cassen 1980). Mantle convection is manifest in the motions of tectonic plates at the Earth's surface (Oxburgh &

Turcotte 1978; Roberts 1987), in the seismically and gravitationally inferred thermal heterogeneity of the Earth's interior (Busse 1983; Dziewonski 1984; Woodhouse & Dziewonski 1984; Dziewonski & Woodhouse 1987) and in the topographic undulations of the core–mantle boundary (Bloxham & Gubbins 1985; Bowin 1986; Creager & Jordan 1986; Morelli & Dziewonski 1987; Olson, Schubert & Anderson 1987). Core–mantle boundary topography suggests coupling of mantle dynamics to flow in the Earth's outer core and to the generation of the geomagnetic field (Gubbins & Richards 1986). The highly nonlinear nature of thermal convection dictates that investigation be done through experiment, either laboratory or numerical. However, the laboratory simulation of a central gravity field is sufficiently difficult (cf. Hart, Glatzmaier & Toomre 1986) that numerical experimentation must be the primary tool for exploration of convection in spherical systems.

The majority of numerical analysis done on infinite Pr convection in spherical shells (see review by Machetel & Yuen 1988) has assumed axisymmetry (Hsui, Turcotte & Torrance 1972; Zebib, Schubert & Straus 1980; Schubert & Zebib 1980; Zebib *et al.* 1983; Zebib, Goyal & Schubert 1985; Machetel & Rabinowicz 1985; Machetel & Yuen 1986, 1987). However, analytic studies (Busse 1975; Busse & Riahi 1982) and stability analyses (Zebib *et al.* 1980; Schubert & Zebib 1980; Zebib *et al.* 1983, 1985; Bercovici, Schubert & Zebib 1988) indicate that there are only a limited number of axisymmetric solutions that are stable to three-dimensional (i.e. azimuthal) perturbations. In addition, the stability of solutions is strongly dependent on the shell thickness and mode of heating; for a shell entirely heated from within, no axisymmetric solutions have yet been found that are stable to azimuthal perturbations (Schubert & Zebib 1980; Bercovici *et al.* 1988). Even when an axisymmetric solution is stable, it is not necessarily a preferred solution to the full equations of motion (Young 1974). Only recently, with the advent of supercomputers, have strongly nonlinear, fully three-dimensional solutions been generated (Baumgardner 1985; Glatzmaier 1988). Machetel, Rabinowicz & Bernadet (1986) studied axisymmetric and three-dimensional convective solutions for a shell with constant gravity and an inner to outer radius ratio of 0.62. They examined the multiplicity of nonlinear solutions that exist for a variety of initial conditions at a slightly supercritical Rayleigh number Ra. For Ra as high as $13Ra_{cr}$ (Ra_{cr} is the critical Ra for the onset of convection), they found that only 'polygonal' type solutions are stable. One such solution is similar to the 'cubic' solution found in this paper.

This work presents nonlinear convective solutions for a spherical shell with properties characteristic of the Earth's whole mantle for Rayleigh numbers up to 70000 (approximately $100Ra_{cr}$). To validate the solutions, we have compared the results of two independently developed numerical codes for several test cases. Two distinct convective patterns arise in these numerical experiments: cubic and tetrahedral. These patterns are closely related to the geometric planforms predicted by analytical theories of slightly supercritical spherical convection (Busse 1975; Busse & Riahi 1982). We present a quantitative analysis of the horizontal and vertical structures of the velocity and temperature fields of these solutions and examine their heat transport properties, including the total heat flow and the spatial distribution of the heat flux at the shell boundaries. Because the small-amplitude analytic theory predicts patterns of convection that are independent of flow direction, we test the stability of the finite-amplitude convective patterns to flow reversal.

2. Mathematical theory

The two numerical codes used in this paper follow different theoretical formulations. One code uses a Boussinesq approximation in which incompressibility is assumed for all but the buoyancy force in the momentum equation. The other code employs an anelastic approximation in which the mass flux vector (instead of velocity) is assumed solenoidal. The anelastic code accordingly treats density stratification and adiabatic and viscous heating; acoustic oscillations are neglected. Application of the anelastic code in this paper will be limited to Boussinesq cases. The Boussinesq code uses a fully Galerkin spectral method and shall henceforth be referred to as the BG code. The anelastic code employs a spectral-transform, Chebyshev collocation scheme and will be called the AS code.

The non-dimensional equations of mass, momentum and energy used by the BG code for an infinite Pr, constant viscosity, constant gravity, spherical fluid shell are

$$\nabla \cdot \boldsymbol{v} = 0, \tag{2.1}$$

$$\nabla^2(\nabla \times \boldsymbol{v}) + Ra\nabla \times (\Theta \boldsymbol{r}/r) = 0, \tag{2.2}$$

$$\frac{\partial \Theta}{\partial t} + \boldsymbol{v} \cdot \nabla(\Theta_c + \Theta) = \nabla^2 \Theta, \tag{2.3}$$

where $\boldsymbol{v}$ is the velocity vector, $\boldsymbol{r}$ is the radius vector and Θ is the temperature perturbation to the conductive temperature profile Θ_c which is the solution of

$$\frac{1}{r^2}\frac{\partial}{\partial r}\left(r^2 \frac{\partial \Theta_c}{\partial r}\right) = -\epsilon, \tag{2.4a}$$

$$\Theta_c = 0 \quad \text{at } r = r_2, \quad \Theta_c = 1 \quad \text{at } r = r_1, \tag{2.4b}$$

(r_1 and r_2 are, respectively, the inner and outer radii of the shell and $r_1/r_2 = 0.55$, a value typical of the Earth's whole mantle). In this study we only consider a shell heated from below and hence the dimensionless internal heating parameter ϵ is zero. The Rayleigh number Ra is defined as

$$Ra = \frac{g\alpha \Delta T d^3}{\nu \kappa}, \tag{2.5}$$

where g is the constant gravitational acceleration, α is the coefficient of thermal expansion, ΔT is the temperature drop across the shell, d is the thickness of the shell, ν is the kinematic viscosity and κ is the thermal diffusivity. All physical parameters are assumed constant throughout the layer. Time t is non-dimensionalized by d^2/κ, distance by d, and temperature by ΔT. Equations (2.1)–(2.3) obey isothermal, impermeable and free-slip boundary conditions,

$$\Theta = v_r = \partial^2(rv_r)/\partial r^2 = 0 \quad \text{at } r = r_1, r_2, \tag{2.6}$$

where v_r is the radial component of the velocity. Given the spherically symmetric viscosity and homogeneous boundary conditions, only the poloidal component of the velocity field can exist, and hence

$$\boldsymbol{v} = \nabla \times \nabla \times (\Phi \boldsymbol{r}/r), \tag{2.7}$$

where Φ is a poloidal velocity potential.

Following the Galerkin method of Zebib *et al.* (1980) (see also Ali-Kahn 1982), Θ and Φ are expanded in terms of orthonormal functions

$$\Theta = \sum_{l=0}^{L} \sum_{\beta=0}^{l} \sum_{k=1}^{N} \frac{1}{\mathcal{N}_l^\beta} (\tau_{l\beta k} \cos(\beta\phi) + \vartheta_{l\beta k} \sin(\beta\phi)) P_l^\beta(\cos\theta) \sqrt{2} \sin(k\pi[r-r_1]), \quad (2.8)$$

$$\Phi = Ra \sum_{l=0}^{L} \sum_{\beta=0}^{l} \sum_{k=1}^{N} \frac{1}{\mathcal{N}_l^\beta} (\tau_{l\beta k} \cos(\beta\phi) + \vartheta_{l\beta k} \sin(\beta\phi)) P_l^\beta(\cos\theta) r f_{lk}(r), \quad (2.9)$$

where θ and ϕ are colatitude and longitude, the $\tau_{l\beta k}$ and $\vartheta_{l\beta k}$ are time-dependent expansion coefficients, P_l^β is an associated Legendre polynomial of degree l and order β and the normalization factor is

$$\mathcal{N}_l^\beta = \left(b_\beta \pi \frac{2}{(2l+1)} \frac{(l+\beta)!}{(l-\beta)!} \right)^{\frac{1}{2}}, \quad (2.10)$$

($b_\beta = 1 + \delta_{\beta 0}$, in which δ is the Kronecker delta function). The radial function chosen for Θ directly satisfies the boundary conditions on Θ in (2.6). The radial function f_{lk} is independent of azimuthal order because its generating equations (obtained by substituting (2.8) and (2.9) into (2.7), $\boldsymbol{r} \cdot \nabla \times$ (2.2) and (2.6); see Chandrasekhar 1961; Zebib *et al.* 1980)

$$D_l^2 f_{lk} = \frac{\sqrt{2}}{r} \sin(k\pi[r-r_1]), \quad (2.11a)$$

$$f_{lk} = d^2 f_{lk}/dr^2 = 0 \quad \text{at } r_1, r_2, \quad (2.11b)$$

$$\left(\text{where } D_l[\ldots] = \frac{1}{r^2} \frac{\partial}{\partial r} r^2 \frac{\partial}{\partial r} [\ldots] - \frac{l(l+1)}{r^2} [\ldots] \right)$$

are degenerate in β.

The evolution equation for the $\tau_{l\beta k}$ is obtained by substituting the solutions to (2.11) and the expansions (2.8) and (2.9) into (2.7) and (2.3), multiplying by

$$\frac{1}{\mathcal{N}_m^\delta} (\cos(\delta\phi) P_m^\delta(\cos\theta) \sqrt{2} \sin(j\pi[r-r_1])),$$

and integrating over r, θ and ϕ from r_1 to r_2, 0 to π and 0 to 2π, respectively. The evolution equations for the $\vartheta_{l\beta k}$ are similarly derived (only for $\beta, \delta > 0$) except that $\cos(\delta\phi)$ is replaced by $\sin(\delta\phi)$. This procedure yields two coupled dynamic equations for the $\tau_{l\beta k}$ and $\vartheta_{l\beta k}$ (note that, because of orthogonality, the l, β and k have been replaced by m, δ and j):

$$\frac{\mathrm{d}}{\mathrm{d}t} \tau_{m\delta j} = \sum_k L_{mkj} \tau_{m\delta k} - \sum_{l\beta k} \sum_{n\gamma i} N_{l\beta k n\gamma i m\delta j} (\mathcal{H}_{\beta\gamma\delta} \tau_{l\beta k} \tau_{n\gamma i} + \Psi_{\beta\gamma\delta} \vartheta_{l\beta k} \vartheta_{n\gamma i}), \quad (2.12a)$$

$$\frac{\mathrm{d}}{\mathrm{d}t} \vartheta_{m\delta j} = \sum_k L_{mkj} \vartheta_{m\delta k} - \sum_{l\beta k} \sum_{n\gamma i} N_{l\beta k n\gamma i m\delta j} (\Psi_{\delta\gamma\beta} \tau_{l\beta k} \vartheta_{n\gamma i} + \Psi_{\delta\beta\gamma} \vartheta_{l\beta k} \tau_{n\gamma i}), \quad (2.12b)$$

where

$$L_{mkj} = -Ram(m+1) A_{mkj} + B_{mkj}, \quad (2.13a)$$

$$A_{mkj} = \sqrt{2} \int_{r_1}^{r_2} (f_{mk}/r) \sin(j\pi[r-r_1]) (\mathrm{d}\Theta_c/\mathrm{d}r)\, \mathrm{d}r, \quad (2.13b)$$

$$B_{mkj} = 2 \int_{r_1}^{r_2} \sin(j\pi[r-r_1]) D_m(\sin(k\pi[r-r_1]))\, \mathrm{d}r, \quad (2.13c)$$

$$N_{l\beta k\alpha i m\delta j} = Ra(l(l+1)\,C_{lijk} + a_{\ell nm} D_{lijk})\,G^{\beta\gamma\delta}_{\ell nm}, \tag{2.14a}$$

$$C_{lijk} = 2\int_{r_1}^{r_2} (f_{lk}/r)\, i\pi \cos(i\pi[r-r_1]) \sin(j\pi[r-r_1])\,\mathrm{d}r, \tag{2.14b}$$

$$D_{lijk} = 2\int_{r_1}^{r_2} \frac{1}{r}\frac{\mathrm{d}}{\mathrm{d}r}(rf_{lk}) \sin(i\pi[r-r_1]) \sin(j\pi[r-r_1])\,\mathrm{d}r, \tag{2.14c}$$

$$a_{\ell nm} = \tfrac{1}{2}(\ell(\ell+1) + n(n+1) - m(m+1)), \tag{2.14d}$$

$$G^{\beta\gamma\delta}_{\ell nm} = \int_{-1}^{+1} p^\beta_\ell\, p^\gamma_n\, p^\delta_m\, \mathrm{d}(\cos\theta), \tag{2.14e}$$

(in which $p^\beta_\ell = (b_\beta \pi)^{\frac{1}{2}} P^\beta_l / \mathscr{N}^\beta_l$),

$$\mathscr{K}_{\beta\gamma\delta} = (b_\beta b_\gamma b_\delta \pi^3)^{-\frac{1}{2}} \int_0^{2\pi} \cos(\beta\phi)\cos(\gamma\phi)\cos(\delta\phi)\,\mathrm{d}\phi, \tag{2.14f}$$

$$\Psi_{\beta\gamma\delta} = (b_\delta \pi^3)^{-\frac{1}{2}} \int_0^{2\pi} \sin(\beta\phi)\sin(\gamma\phi)\cos(\delta\phi)\,\mathrm{d}\phi. \tag{2.14g}$$

From (2.12), one can see that solutions initiated with even symmetry about $\phi = 0$ (i.e. with $\vartheta_{l\beta k} = 0$) will remain symmetric. However, none of the solutions in this paper is initiated with this special symmetry. Nevertheless, the solutions obtained here do exhibit even symmetry about at least one plane of constant ϕ, though not necessarily $\phi = 0$.

The AS code employs the dimensional anelastic equations of motion (again, $Pr = \infty$)

$$\boldsymbol{\nabla} \cdot (\bar{\rho}\boldsymbol{v}) = 0, \tag{2.15}$$

$$-\boldsymbol{\nabla}P' + \boldsymbol{\nabla}\cdot\boldsymbol{\sigma} - \rho' g \boldsymbol{r}/r = 0, \tag{2.16}$$

$$\bar{\rho}\bar{T}\left(\frac{\partial S'}{\partial t} + \boldsymbol{v}\cdot\boldsymbol{\nabla}S'\right) = \boldsymbol{\nabla}\cdot(k\boldsymbol{\nabla}(\bar{T}+T')) + Q + \boldsymbol{\sigma}:\boldsymbol{e}. \tag{2.17}$$

Density is decomposed into $\bar{\rho}(r)$, the basic state, hydrostatic, adiabatic, polytropic density profile based on the Murnaghan equation of state (Stacey 1977; Glatzmaier 1988), and $\rho'(r,\theta,\phi,t)$, the superadiabatic perturbation density, related to P', the pressure perturbation, and S', the specific entropy perturbation through a first-order Taylor expansion with Maxwell's relations. Temperature is decomposed into $\bar{T}$ and T' in the same fashion as ρ. The superadiabatic perturbations include the effects of the superadiabatic conductive state that would exist if convection was prohibited. The strain rate tensor $\boldsymbol{e}$ has its classical definition and the stress tensor $\boldsymbol{\sigma} = 2\bar{\rho}\nu\boldsymbol{e}$. For this study, the internal heating density Q is set to zero and the thermal conductivity k is assumed constant. The mass flux is solenoidal, hence

$$\bar{\rho}\boldsymbol{v} = \boldsymbol{\nabla}\times\boldsymbol{\nabla}\times(W\boldsymbol{r}/r) + \boldsymbol{\nabla}\times(Z\boldsymbol{r}/r),$$

where W and Z are, respectively, the poloidal and toroidal mass flux potentials. Again, because viscosity is assumed constant and the boundary conditions are homogeneous, $Z = 0$.

The non-dimensional number measuring the degree of compressibility is the dissipation number Di, equal to the ratio of the thickness of the fluid layer to the adiabatic temperature scale height, that is, $Di = (\alpha g d)/c_p$. In the simplest form of compressibility, Di and the Grüneisen parameter γ (where $\gamma = (\rho/T)(\partial T/\partial\rho)_s =$

$(\alpha K_s)/(\rho c_p)$ and K_s is the bulk modulus) are constant. In this case, the adiabatic temperature $\bar{T} = \bar{T}_0 \exp(-Di[r-r_0]/d)$ and density $\bar{\rho} = \bar{\rho}_0 \exp(-[Di/\gamma][r-r_0]/d)$, where $\bar{T}_0$ and $\bar{\rho}_0$ are reference adiabatic temperature and density at a radius r_0. Assuming that dynamic viscosity η and specific heat c_p (in addition to thermal conductivity k) are constant through the shell, one may non-dimensionalize time by $(\bar{\rho}_0 c_p d^2)/k$, distance by d, pressure and stress by $\eta k/(\bar{\rho}_0 c_p d^2)$, entropy by $c_p \Delta T/\bar{T}_0$ and the temperature perturbation by ΔT (where ΔT is the superadiabatic temperature drop across the shell). Use of these scales to non-dimensionalize (2.15)–(2.17) yields

$$\nabla \cdot \boldsymbol{u} = \frac{-Di}{\gamma} u_r, \tag{2.15'}$$

$$0 = \nabla P' + \nabla^2 \boldsymbol{u} - \frac{1}{3}\frac{Di}{\gamma}\nabla u_r + \frac{\bar{\rho}\bar{T}}{\bar{\rho}_0 \bar{T}_0} RaS'\boldsymbol{r}/r - \frac{Di}{\gamma} P'\boldsymbol{r}/r, \tag{2.16'}$$

$$\frac{\bar{\rho}\bar{T}}{\bar{\rho}_0 \bar{T}_0}\left(\frac{\partial S'}{\partial t} + \boldsymbol{v}\cdot\nabla S'\right) = \nabla^2(\bar{T}/\Delta T + T') + \frac{Di}{Ra}\boldsymbol{\sigma}:\boldsymbol{e}, \tag{2.17'}$$

where $T' = (\bar{T}/\bar{T}_0)S' + (\bar{\rho}_0/\bar{\rho})\alpha\bar{T}(Di/Ra)P'$ and Ra is with respect to kinematic viscosity and thermal diffusivity at r_0. All dependent and independent variables are non-dimensional while the adiabatic temperature $\bar{T}$ and density $\bar{\rho}$ are treated as material properties and hence are left dimensional. In this paper, Di is set equal to zero, which recovers the Boussinesq case exactly.

The dependent variables, W, S' and P' are represented in terms of spherical harmonics and Chebyshev polynomials, for example,

$$W = (2/N)^{\frac{1}{2}} \sum_{l=0}^{L} \sum_{m=-l}^{+l} \sum_{n=0}^{N} W_{lmn}(1-\tfrac{1}{2}(\delta_{n0}+\delta_{nN}))\, T_n(x)\, Y_l^m, \tag{2.18}$$

where

$$x = 2\left(\frac{r-r_1}{r_2-r_1}\right) - 1, \tag{2.19a}$$

$$T_n(x) = \cos(n\cos^{-1}x), \tag{2.19b}$$

$$Y_l^m = \left(\frac{2l+1}{4\pi}\frac{(l-m)!}{(l+m)!}\right)^{\frac{1}{2}} P_l^m(\cos\theta)\, e^{im\phi}, \tag{2.19c}$$

and the W_{lmn} are complex, time-dependent expansion coefficients. To ensure that W (as well as S' and P') is real,

$$W_{l(-m)n} = (-1)^m W_{lmn}^*, \tag{2.19d}$$

since $Y_l^{-m} = (-1)^m Y_l^{m*}$. The spectral representation resulting from substitution of the above expansion into (2.15)–(2.17) will not be shown since the AS code solves the equations of motion as much in physical space as in spectral space.

3. Methods of solution

The BG code solves the initial-value problem presented by (2.12) with an implicit time integration scheme based on stability analysis. The nonlinear interaction of modes is fully accounted for within truncation levels. Small wavelength disturbances that are unresolved are merely truncated and not folded back into the large wavelength modes, which would lead to aliasing. With the implicit time integration,

all spectral coefficients (i.e. $\tau_{l\beta k}$ and $\vartheta_{l\beta k}$) are coupled. Thus, a linear system of equations of order equal to the total number of coefficients must be solved at least once per timestep; for a moderate resolution of $L = 10$ and $N = 8$, this system of equations is approximately of order 1000, requiring almost 10^6 words of memory. However, an advantage of the implicit scheme is its unconditional stability such that the timestep is usually two orders of magnitude greater than that for an explicit scheme and, when a steady solution is approached, the timestep can grow without bound. (However, if a solution is inherently oscillatory or chaotic, its time-dependence may be suppressed unless the timestep satisfies the Courant condition.) Steadiness of a solution is assumed when the maximum fractional change of the coefficients over a timestep is less than or equal to 10^{-6}. A more thorough discussion of the computational technique can be found in Zebib *et al.* (1980).

The AS code solves the equations of motion with a semi-implicit scheme; the nonlinear terms are treated explicitly with an Adams–Bashforth method and the linear terms treated implicitly with a Crank–Nicolson scheme. The nonlinear terms of two adjacent time levels are calculated in physical space and transformed to spectral space via fast Fourier transforms (for radial and azimuthal dependences) and Gaussian quadrature (for latitudinal dependence) whereupon the spectral coefficients of the dependent variables are found at the next time level from the equations of motion and energy. This allows for partial decoupling of the coefficients and hence faster solution of the system of equations as well as much less memory. Also, since only the linear terms are implicit, the matrix inversion for each l need only be done once for a given timestep size. However, with a partially explicit scheme, the timestep is highly constrained and must always satisfy the Courant condition for convective velocities. The aliasing of modes is reduced by calculating the nonlinear terms on a physical space grid with the number of nodal points in excess of that necessary to complete a discrete transform of the linear terms; the transform of nonlinear terms to spectral space is done with all the grid points and the resulting modes that are above the truncation level are dropped. A more complete discussion of the AS code can be found in Glatzmaier (1984, 1988).

Since the two codes use different radial expansions for the spectral representation, their radial resolutions will be different, even if the expansions are of similar degree. The density of Chebyshev collocation grid points varies as $1/N^2$ near the boundaries and $1/N$ at the middle of the shell. The comparable points for a sine series (i.e. the zeros or the extrema of the smallest wavelength term of the series) have a density that varies as $1/N$ uniformly through the shell. This implies that the Chebyshev series can resolve boundary layers at the top and bottom of the shell better than the sine series.

4. Verification of methods

Four Boussinesq comparison test cases were run with both numerical codes in order to establish their validity. The test cases involve axisymmetric convection at $Ra = 14250$ and fully three-dimensional convection at $Ra = 2000$, 3500 and 7000. Given that the minimum critical Rayleigh numbers for odd and even l are $Ra_{cr} = 712$ for $l = 3$ and $Ra_{cr} = 729$ for $l = 4$ (Bercovici *et al.* 1988), these Rayleigh numbers are, respectively, about 20, 3, 5 and 10 times Ra_{cr}. At these values of Ra, all solutions are at steady state (time-dependence for an $l = 2$ dominant axisymmetric solution occurs at $Ra \approx 30Ra_{cr}$ according to Machetel & Yuen 1986).

Because the BG code is the more cumbersome of the two programs, it dictates the

	$\langle\Theta^2\rangle$	
l	BG	AS
2	1.0	1.0
4	7.010×10^{-2}	7.061×10^{-2}
6	1.001×10^{-1}	1.019×10^{-1}
8	1.197×10^{-2}	1.202×10^{-2}
10	2.703×10^{-2}	2.826×10^{-2}
12	2.055×10^{-3}	2.130×10^{-3}
14	3.857×10^{-3}	4.275×10^{-3}
16	1.439×10^{-4}	1.899×10^{-4}
18	4.473×10^{-4}	6.320×10^{-4}

TABLE 1. Variances of temperature (or entropy) for spherical harmonic degrees $l = 1$ to 18 for the axisymmetric comparison test case at $Ra = 14250$ for both the BG and AS codes. All variances are normalized to the maximum value of $\langle\Theta^2\rangle$.

maximum level of truncation at which the comparison test cases are run. Thus, the maximum N (the radial truncation level) used for the three-dimensional cases is 10. This unfortunately imposes limitations on the AS code since Chebyshev expansions are not efficient for $N < 30$. With such a low N, the AS code tends to be noisy. Thus, steadiness of a solution is defined slightly differently for the AS code than for the BG code; a steady solution is attained when the maximum fractional change in expansion coefficients whose amplitudes are above the level of machine noise is less than or equal to 10^{-6}. The machine noise level is defined as 10^{-9} (for double precision on an IBM 3090 or single precision on a Cray XMP) of the absolute value of the coefficient with maximum amplitude.

For the axisymmetric case, an axisymmetric version of the BG code requires truncation levels of $L = 18$ and $N = 16$ for a 2.5% error between Nusselt numbers Nu at the top and bottom of the shell (Nu is equal to the ratio of spherically averaged total heat flow to conductive heat flow). The Nusselt number at the top of the shell is 3.9778. The solution at $Ra = 14250$ has a two-cell ($l = 2$ dominant) configuration with downwelling at the equator; a similar solution was found by Machetel & Rabinowicz (1985). The AS code obtains the same solution using truncation levels of $L = 19$ and $N = 16$ with less than 1% error in Nu. (The values of L and N for the two codes cannot always be matched exactly since the AS code has restrictions on L and N owing to use of the fast Fourier transform.) The error in heat flow is less for the AS code because, as stated previously, the Chebyshev collocation points allow for greater resolution of boundary layers. The Nu for the AS code is 3.9776.

Table 1 shows temperature (or entropy) variances $\langle\Theta^2\rangle$ (brackets indicate volume averages) for the even spherical harmonic degrees $l = 2$ to 18 (the solution is purely equatorially symmetric) for both codes. The variances are normalized to the maximum value of $\langle\Theta^2\rangle_l$, and the $l = 0$ mode is not listed since its correlation is implied by the agreement of Nusselt numbers (which represent the spherically symmetric temperature field). In this paper, the spectral content of solutions is only discussed in terms of $\langle\Theta^2\rangle$ since, for a spherically symmetric viscosity, the only other relevant spectral energy, i.e. kinetic energy, derives from velocity which is a linear function of temperature (or entropy).

For the three-dimensional cases, the BG code requires $L = 10, N = 8$ for $Ra = 2000$ and 3500, and $L = 10, N = 10$ for $Ra = 7000$. To match the resolution of the BG code

	BG			AS		
Ra	Nu_{top}	Nu_{bot}	% error	Nu_{top}	Nu_{bot}	% error
2000	2.3257	2.2191	4.8	2.2507	2.2532	0.1
3500	2.8106	2.6520	5.9	2.7954	2.7568	1.4
7000	3.6171	3.4593	4.5	3.4657	3.5293	1.8

TABLE 2. Nusselt numbers at the top and bottom of the spherical shell (and the resulting percentage error) for the three-dimensional comparison test cases for both the BG and AS codes.

			$\langle\Theta^2\rangle$	
	l	m	BG	AS
$Ra = 2000$	2	0	1.006×10^{-1}	1.014×10^{-1}
	3	2	1.0	1.0
	4	0	6.253×10^{-2}	6.525×10^{-2}
	4	4	3.564×10^{-1}	3.630×10^{-1}
	6	0	7.740×10^{-3}	7.602×10^{-3}
	6	4	1.149×10^{-2}	1.135×10^{-2}
	7	2	1.152×10^{-2}	1.169×10^{-2}
	7	6	1.784×10^{-2}	1.809×10^{-2}
	8	4	5.381×10^{-3}	5.465×10^{-3}
	8	8	9.609×10^{-3}	9.852×10^{-3}
$Ra = 3500$	4	0	1.0	1.0
	4	4	7.142×10^{-1}	7.143×10^{-1}
	6	0	6.557×10^{-3}	6.702×10^{-3}
	6	4	4.587×10^{-2}	4.692×10^{-2}
	8	0	5.465×10^{-2}	5.576×10^{-2}
	8	4	1.547×10^{-2}	1.577×10^{-2}
	8	8	3.589×10^{-2}	3.661×10^{-2}
	10	0	3.434×10^{-3}	3.417×10^{-3}
	10	4	6.969×10^{-3}	6.940×10^{-3}
	10	8	9.868×10^{-3}	9.832×10^{-3}
$Ra = 7000$	3	2	1.0	1.0
	4	0	1.202×10^{-1}	1.202×10^{-1}
	4	4	8.586×10^{-2}	8.588×10^{-2}
	6	4	1.907×10^{-2}	1.902×10^{-2}
	7	2	1.704×10^{-2}	1.701×10^{-2}
	7	6	1.442×10^{-2}	1.439×10^{-2}
	9	6	3.895×10^{-2}	3.902×10^{-2}
	10	0	9.381×10^{-3}	9.431×10^{-3}
	10	4	1.906×10^{-2}	1.915×10^{-2}
	10	8	2.700×10^{-2}	2.713×10^{-2}

TABLE 3. Variances of temperature (or entropy) for the ten largest modes of spherical harmonic degree l and azimuthal order m for the fully three-dimensional cases at $Ra = 2000$, 3500 and 7000 for both the BG and AS codes. All variances are normalized to the maximum value of $\langle\Theta^2\rangle$.

as closely as possible, the AS code uses $L = 10$, $N = 8$ for the two lower values of Ra and $L = 10$, $N = 12$ for $Ra = 7000$.

All steady solutions are first generated by the BG code. They are then transformed to the representation employed by the AS code and used as initial conditions by the AS code for a time integration. In all cases, a steady state is rapidly found and the AS code successfully maintains the solutions of the BG code.

Table 2 summarizes the values of Nu at the top and bottom of the shell for both codes and all three values of Ra. The Nu range of the BG code either contains that of the AS code or strongly overlaps it. The error in Nu for the BG code is substantial because the solutions are underresolved radially for this code. The energy spectrum of the sine series radial expansion drops less than two orders of magnitude from the largest wavelength to the smallest; hence, truncation error is significant. Alternatively, the energy spectrum of the Chebyshev series drops four orders of magnitude. The ten largest temperature (or entropy) variances $\langle \Theta^2 \rangle_{lm}$ of both codes are listed in table 3, showing the close agreement of results. (Again, the $l = 0$ mode is not listed because its information is redundant with the Nu comparison.) The successful comparison of results from the tests of the two codes offers sound verification of the methods used in our numerical experiments.

5. Nonlinear three-dimensional solutions and the patterns of convection

The nonlinear three-dimensional solutions generated in the comparison tests of the codes are characterized by two different convective patterns. The solutions at $Ra = 2000$ and 7000 are odd solutions (i.e. non-equatorially symmetric) and have a tetrahedral symmetry. The solution at $Ra = 3500$ is even (equatorially symmetric) and has cubic symmetry. Additional calculations presented in this section show that both patterns of convection exist for $712 \leqslant Ra \leqslant 70000$. Figure 1 illustrates the geometric planforms of the two patterns by showing the three-dimensional isothermal (or isentropic) surfaces defined by constant values of

$$\Theta_c + \Theta = \frac{S' - S'_{\text{top}}}{S'_{\text{bottom}} - S'_{\text{top}}}, \tag{5.1}$$

for three Rayleigh numbers in the aforementioned range. Since a fluid parcel undergoing convective transport moves virtually adiabatically (or isothermally for the Boussinesq case), these surfaces are very close to material surfaces, especially at high Ra. The protrusions represent upwelling regions or plumes, while the apparent canyons are downwelling areas. If the upwelling regions are assumed to mark the apexes of a polyhedron, then the odd solution forms a tetrahedron and the even one is an octahedron. We will refer to the odd solution as tetrahedral and the even one as cubic (to denote a certain family of polyhedrons with cubic symmetry to which the octahedron belongs). All solutions have even symmetry about at least two planes of constant ϕ (the cubic pattern has four such planes), although not necessarily about $\phi = 0$, which is an arbitrary coordinate. Both tetrahedral and cubic patterns exist because the two smallest Ra_{cr} occur at $l = 3$ and $l = 4$ and differ by very little (see previous section); at convective onset (for $Ra > 730$), both patterns have nearly equal likelihood of occurring, and one pattern is not preferred over the other.

The convective solutions shown in figure 1, as well as other solutions discussed later in this paper, were obtained with the AS code using the truncation $L = 21$, $N = 16$ for $712 \leqslant Ra \leqslant 14000$ and $L = 31, N = 18$ for $14000 \leqslant Ra \leqslant 70000$. The radial (Chebyshev) energy spectrum of the solutions always falls at least five orders of magnitude and the horizontal (spherical harmonic) energy spectrum falls four orders of magnitude or more (figure 2). Time dependence was not found in the range of Rayleigh numbers investigated. (Even tests with $N = 20$ at $Ra = 70000$ did not yield time-dependence.) Although the solutions appear adequately resolved in time and space, the onset of time-dependence for $Ra \leqslant 70000$ cannot be precluded until

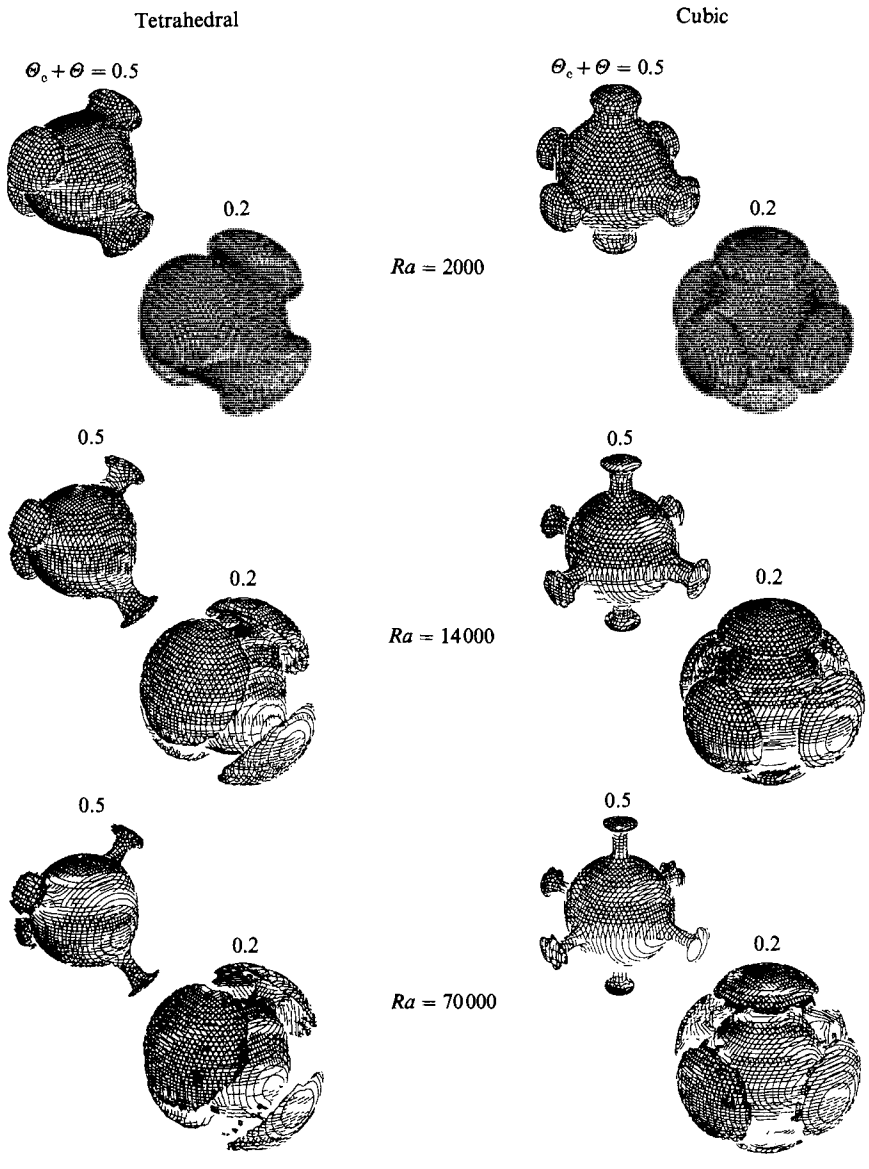

FIGURE 1. Three-dimensional isothermal (or isentropic) surfaces for tetrahedral and cubic patterns of convection for $Ra = 2000$, 14000 and 70000. Two surfaces are shown for each case: one for $\Theta_c+\Theta = 0.5$ and the other for $\Theta_c+\Theta = 0.2$.

further analyses with higher spatial resolution are performed. For $Ra > 35000$, the solutions have a slow asymptotic approach to steady state, i.e. global characteristics (e.g. Nu) of the solutions change monotonically and almost insignificantly after long time integrations, without any variation in the convective pattern. As Ra approaches 70000, transients at the start of the time integrations require more time to decay away, implying that growth rates for oscillatory modes are approaching zero at $Ra = 70000$. If time dependence does not in fact occur within the Ra range of this study, it may set in for Ra not much greater than about $100Ra_{cr}$. Axisymmetric solutions undergo time-dependent, even chaotic motion, at considerably smaller Rayleigh numbers (Machetel & Yuen 1986, 1987).

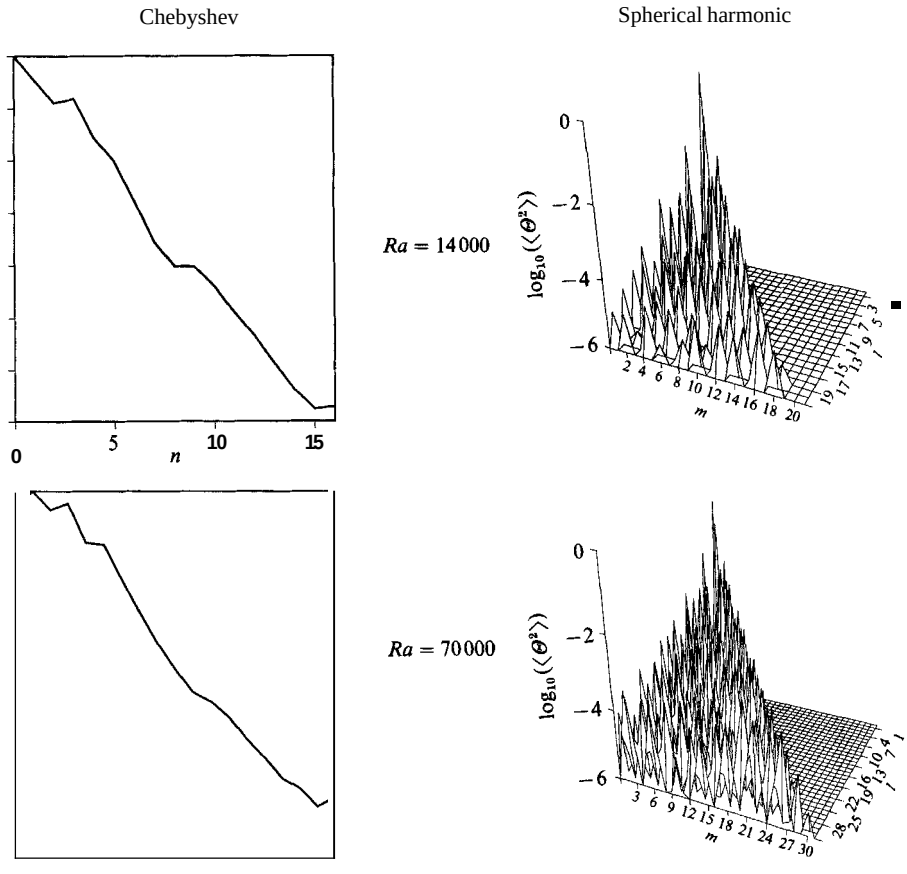

5.1. *Comparison with analytic theory*

Both the cubic and tetrahedral patterns were predicted by the perturbation analyses of Busse **(1975)** and Busse & Riahi (1982), respectively. If two or more dominant spherical harmonic modes exist within a convective pattern, then it is possible to compare the relative energies of these modes from our numerical results with those from the analytic studies. However, the tetrahedral solution has only one dominant mode (for $l = 3, m = 2$); thus, a quantitative comparison of modes cannot be done for this case.

The cubic pattern, predicted by Busse (1975) (and also found numerically by Young (1974) and Machete1 *et al.* (1986))has two dominant modes ($l = 4, m = 0$ and $l = 4, m = 4$), and hence a quantitative comparison is possible. The perturbation analysis (Busse 1975) represents a dependent variable, say Θ, for a given l as

$$\Theta_l = g_l(r) \sum_{m=0}^{l} \alpha_m \cos(m\phi) P_l^m(\cos\theta), \tag{5.2}$$

with the appropriate normalization, and even symmetry about $\phi = 0$ assumed. For the cubic solution, the only non-zero α_m predicted by the theory are

$$\alpha_0 = \tfrac{1}{2}(\tfrac{7}{3})^{\frac{1}{2}}, \quad \alpha_4 = \tfrac{1}{2}(\tfrac{5}{3})^{\frac{1}{2}}, \tag{5.3}$$

for $l = 4$. The ratio of the volume-averaged spectral energies or variances of these two modes is $(\alpha_4/\alpha_0)^2 = \frac{5}{7}$, since $g_l(r)$ is independent of m. This number is unaffected by the assumption of symmetry about $\phi = 0$ since the origin of the longitudinal grid ($\phi = 0$) is arbitrary, and, the solution displays symmetry about four planes of constant ϕ, let alone one. Examination of the volume-averaged variances of the numerical solutions in table 3 for $Ra = 3500$ shows that $\langle \Theta^2 \rangle_{4,4}$, which is normalized by $\langle \Theta^2 \rangle_{4,0}$, is also $\frac{5}{7}$. This ratio is in fact maintained for Ra up to 70000, although other small wavelength modes become more significant. Machetel *et al.* (1986) also found that the relative importance of modes for their 'polygonal P44' (cubic) solution remained essentially unaltered up to $13Ra_{\mathrm{cr}}$.

Polygonal patterns are the spherical analogues of hexagonal patterns in plane layer convection (axisymmetric patterns are analogous to plane layer convective rolls). Since convection in a fluid layer without midplane symmetry can only have a hexagonal planform (Busse 1978), Busse (1975) predicts that the polygonal convective patterns in a spherical shell (lacking midplane symmetry) would be the only stable patterns, and would exist for Rayleigh numbers much greater than the slightly supercritical Ra used in small-amplitude theory. Our results verify this prediction.

As is evident from table 3 for $Ra = 7000$, the tetrahedral solution has, along with the dominant $\langle \Theta^2 \rangle_{3,2}$ variance, small yet significant $\langle \Theta^2 \rangle_{4,4}$ and $\langle \Theta^2 \rangle_{4,0}$ variances; the ratio of these two minor variances is also $\frac{5}{7}$. The tetrahedral solution is, in fact, a mixed-mode solution that combines a dominant tetrahedral signature with a small cubic signature. This mixed-mode solution was predicted by Busse & Riahi (1988). However, the radial function of the analytic solution ($g_l(r)$ in (5.2)) is dependent on l and must therefore be known (or at least the integral of its square over the volume of the shell must be known) in order to calculate the relative variances of the mixed-mode solution. The analytic work does not explicitly determine the radial function and hence a quantitative comparison of the analytic solution with our numerical results cannot be done.

6. Three-dimensional structure of convective solutions

6.1. *Horizontal structure of velocity and temperature fields*

Radial velocity and temperature anomaly contours midway through the shell are shown in figures 3 and 4, respectively, to quantify the horizontal structure of the three-dimensional patterns. The figures additionally illustrate how the structure changes with increasing Ra. For both the tetrahedral and cubic patterns, the upwelling areas are cylindrical and are separated by downwelling fluid. Although downwelling regions have local extrema, they are usually connected in a network of linear features. This structure is characteristic of the 'polygonal' solutions found by Machetel *et al.* (1986). As Ra increases, the upwelling and downwelling regions become more confined to narrow areas and the virtually stagnant region between them grows in width (i.e. the spacings between the zero-contour and the next nearest contours increase). At high Rayleigh numbers, the downwelling regions are manifest as a network of narrow linear sheets.

Features of the temperature field (especially at $Ra = 70000$) whose horizontal

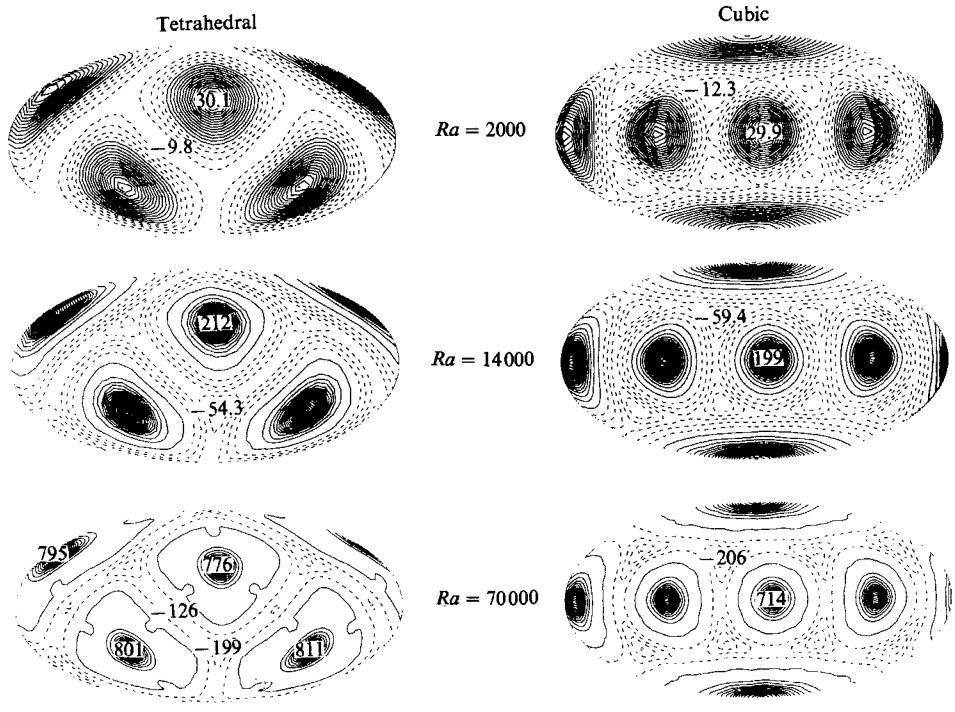

FIGURE 3. Radial velocity contours (in a Hammer–Aitoff equal area projection) of the tetrahedral and cubic patterns on a spherical surface midway through the shell for $Ra = 2000$, 14000 and 70000. Dashed contours indicate downwelling and solid contours denote upwelling; the solid contour separating the negative velocity region from the positive one is the zero value contour. The numerical values are the maximum upwelling and downwelling non-dimensional velocities; the other upwelling and downwelling areas have the same maximum velocities as those shown, unless otherwise indicated. Contouring information is given in table 4(*a*).

dimensions are less than 5° in longitude or latitude are not well resolved and are possibly numerical noise. However, the larger wavelength complex structure surrounding the upwellings at $Ra = 70000$ is well resolved.

At all Ra, and for both patterns, the maximum velocities and temperature anomalies always occur in the upwelling regions. Midway through the shell, the maximum upwelling velocities are three to four times the maximum velocities of the downwelling regions and the magnitudes of the hot temperature anomalies are three to five times the magnitudes of the cold temperature anomalies. However, the horizontal velocity and temperature gradients in the downwelling regions are less than those in the upwelling regions; this accommodates the constraint that surface-averaged velocities and temperature anomalies at any radius must be zero. The velocity and temperature maxima of upwelling are greater for the tetrahedral pattern than for the cubic pattern, while the reverse is true of the downwelling velocity and temperature. For both patterns, as Rayleigh number increases, the maximum (non-dimensional) temperature anomaly of the upwelling region increases, while that of the downwelling region decreases slightly. This probably reflects the narrowing and subsequent intensification of upwelling plumes and the spreading of downwelling fluid more uniformly into sheets. The temperature anomalies of these regions are more detailed than the velocity features because in large Pr systems internal (thermal) energy undergoes much less diffusion than momentum.

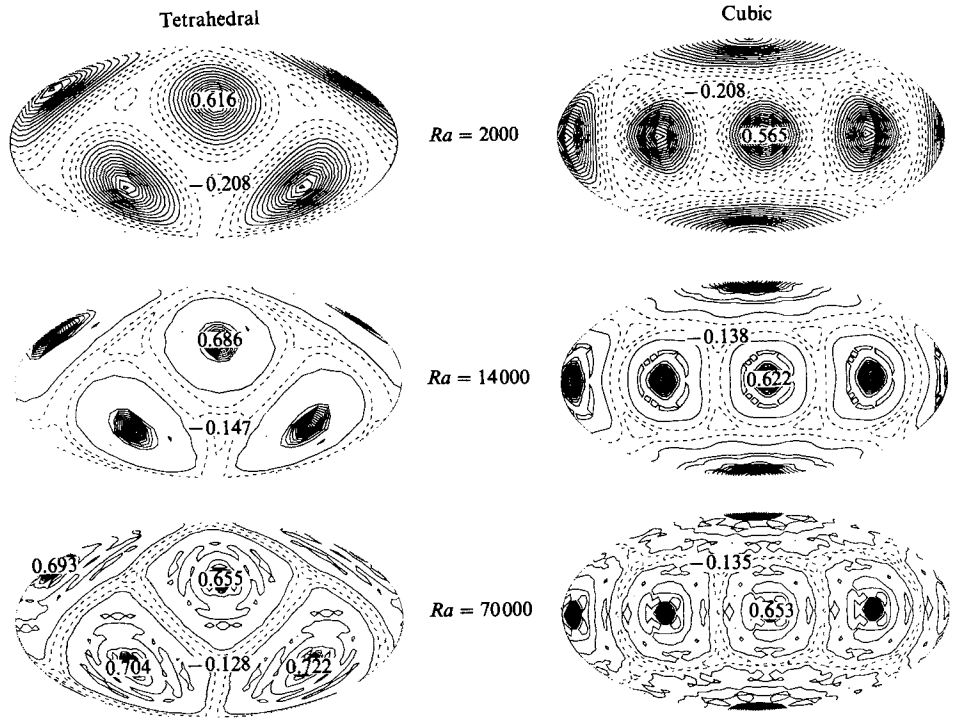

FIGURE 4. Isotherms (in equal area projection) relative to the spherically-averaged temperature on a spherical surface midway through the shell for the same patterns and Rayleigh numbers as in figure 3. Dashed lines are for negative (cold) temperature anomalies and solid lines are for positive (hot) temperature anomalies; the solid contour separating the cold and hot regions is the zero value contour. The maximum hot and cold non-dimensional temperature anomalies are shown; the other upwelling and downwelling regions have the same extremum temperatures unless otherwise indicated. Contouring information is given in table 4(*a*).

For all *Ra*, the velocity and temperature maxima of the upwelling regions coincide. However, for the tetrahedral solution at $Ra = 2000$, the downwelling temperature and velocity maxima do not coincide; the extrema of the downwelling velocity occur at the equator while the extrema of the temperature occur at the same latitude as the upwelling plumes. At higher *Ra*, the downwelling maxima of both temperature and velocity in the tetrahedral solutions occur at the high latitudes. This indicates that at low *Ra* the locations of horizontal flow convergence at the upper boundary are more important in determining the locations of downwelling than are the sites of coldest temperature anomaly; this situation is reversed at higher *Ra*.

For both patterns, the areas of negative radial velocity in the downwelling zones are broader than the corresponding areas of negative (cold) temperature anomalies. Therefore, areas of downwelling overlap areas of relatively warm material. Despite the relative buoyancy of this fluid, it is entrained into the downwelling currents.

The upwelling and downwelling regions of both patterns do not maintain the same horizontal structure throughout the depth of the shell (figure 5). At all Rayleigh numbers, the upwelling regions of the cubic pattern are nearly circular at the top of the shell. Near the middle of the shell the upwelling regions are quite complex, as though undergoing a sharp transition with depth, and at the bottom of the shell they are distinctly in the shape of diamonds. At low *Ra*, the upwelling regions of the

(*a*)

Figure number	Pattern	Rayleigh number	Minimum contour	Maximum contour	Contour interval
3	Tetrahedral	2000	−8	30	2
		14000	−50	210	10
		70000	−180	780	60
	Cubic	2000	−12	30	2
		14000	−50	200	10
		70000	−200	700	50
4	Tetrahedral	2000	−0.2	0.60	0.05
		14000	−0.1	0.65	0.05
		70000	−0.1	0.70	0.05
	Cubic	2000	−0.2	0.56	0.04
		14000	−0.1	0.65	0.05
		70000	−0.1	0.70	0.05
7	Tetrahedral	2000	−0.48	0.48	0.06
		14000	−0.48	0.48	0.06
		70000	−0.18	0.72	0.06
	Cubic	2000	−0.18	0.72	0.06
		14000	−0.48	0.48	0.06
		70000	−0.18	0.72	0.06

(*b*)

Figure number	Pattern	Rayleigh number	Radius (r/r_2)	Minimum contour	Maximum contour	Contour interval
5	Tetrahedral	70000	0.97	−0.15	0.65	0.05
			0.89	−0.15	0.65	0.05
			0.78	−0.10	0.70	0.05
			0.66	−0.10	0.80	0.05
			0.58	−0.30	0.55	0.05
	Cubic	14000	0.97	−0.12	0.52	0.04
			0.89	−0.15	0.60	0.05
			0.78	−0.10	0.70	0.05
			0.66	−0.10	0.75	0.05
			0.58	−0.20	0.40	0.04
		70000	0.97	−0.16	0.60	0.04
			0.89	−0.12	0.60	0.04
			0.78	−0.10	0.70	0.05
			0.66	−0.10	0.75	0.05
			0.58	−0.20	0.60	0.05
10	Tetrahedral	70000	1.00	0	32	2
			0.55	2	22	1
	Cubic	70000	1.00	0	29	1
			0.55	2	21	1

(*c*)

Figure number	Pattern	Function	Minimum contour	Maximum contour	Contour interval
13	Tetrahedral	Radial velocity	−49	70	7
		Temperature	−0.24	0.44	0.04
	Cubic	Radial velocity	−48	80	8
		Temperature	−0.24	0.48	0.04

TABLE 4. Contouring information for figures 3, 4, 7, 5, 10 and 13.

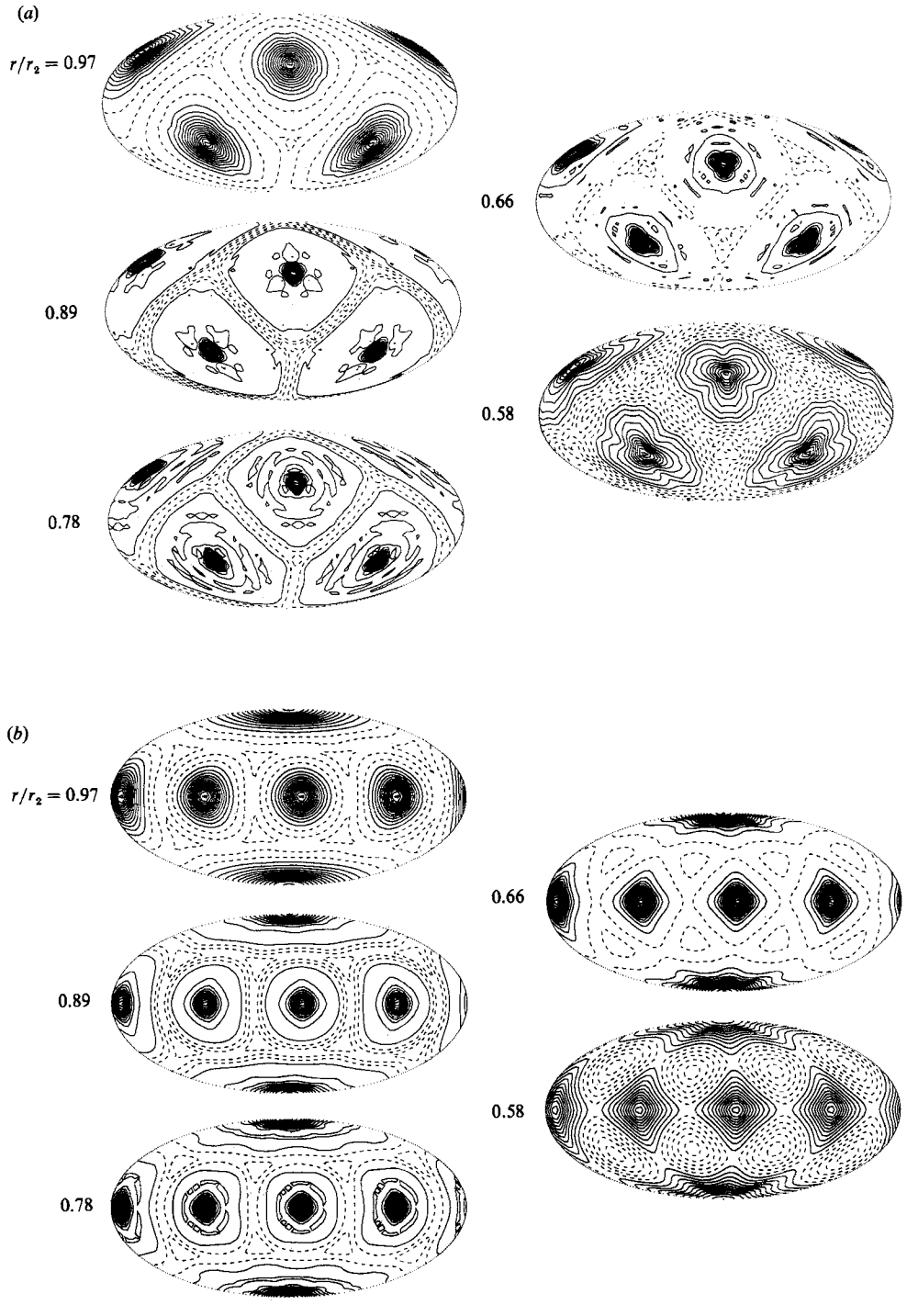

FIGURE 5(*a*, *b*). For caption see next page.

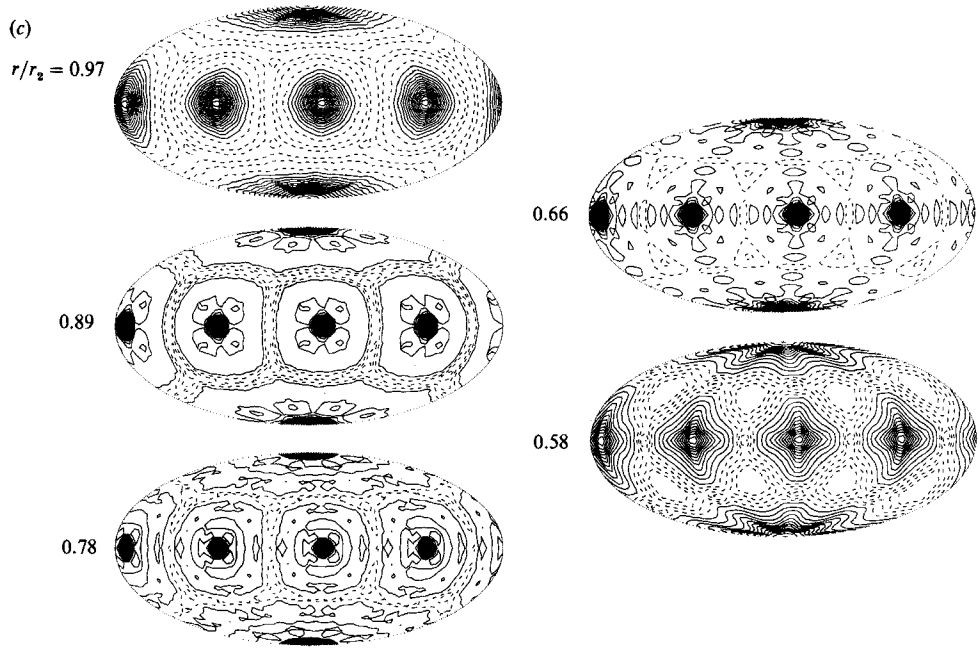

FIGURE 5. Isotherms (in equal area projection) relative to the spherically-averaged temperature for (*a*) the tetrahedral pattern at $Ra = 70000$, (*b*) the cubic pattern at $Ra = 14000$ and (*c*) the cubic pattern at $Ra = 70000$ on five spherical surfaces at radii $r/r_2 = 0.97, 0.89, 0.78, 0.66$ and 0.58; these five radii correspond to depths of 3, 25, 50, 75 and 97% of the shell thickness. Contouring information is given in table 4(*b*).

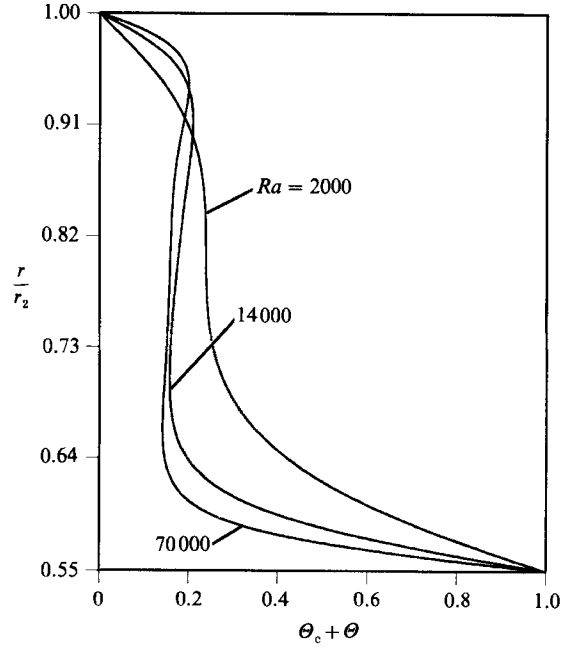

FIGURE 6. Spherically-averaged profiles of total non-dimensional temperature $\Theta_c + \Theta$ at $Ra = 2000$, 14000 and 70000 for the tetrahedral pattern (the profiles of the cubic pattern are essentially identical).

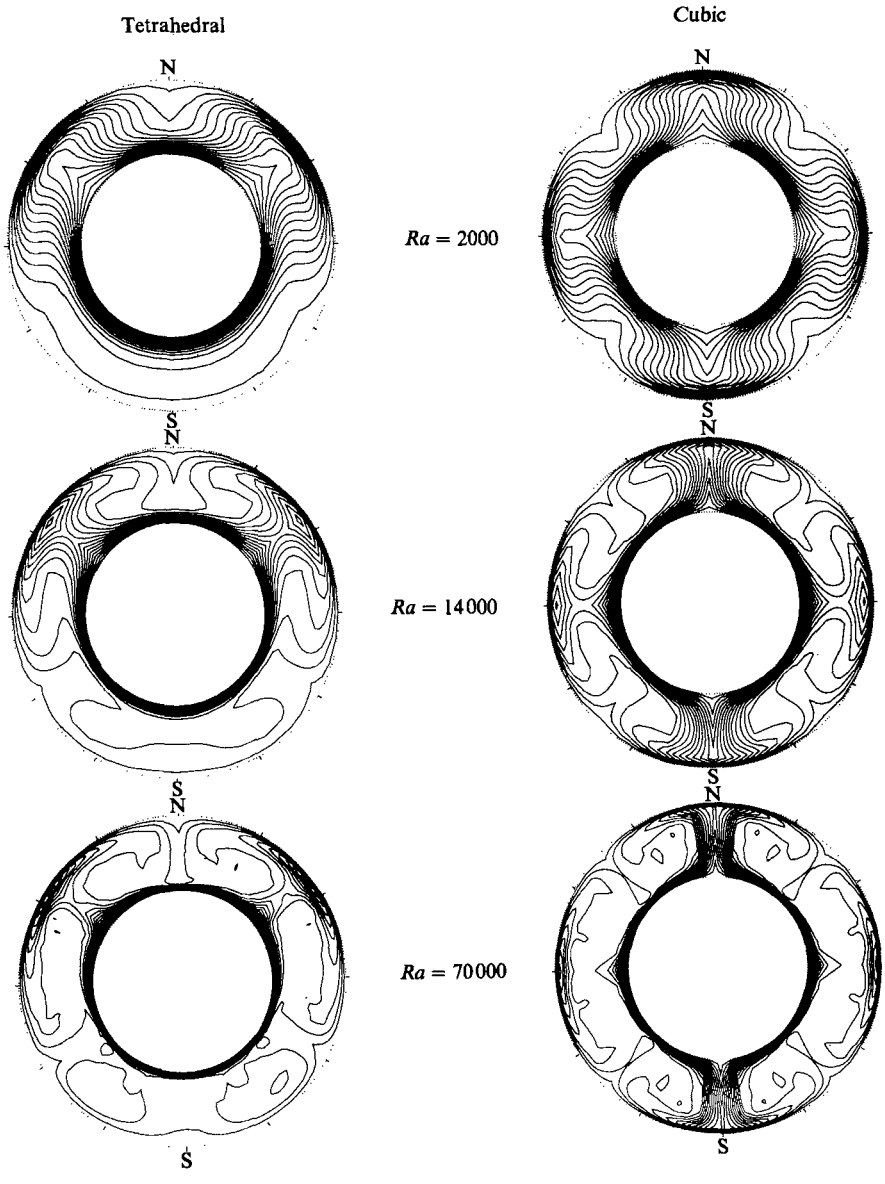

FIGURE 7. Isotherms of total temperature in a vertical plane of constant longitude ($\phi = 0$) for the tetrahedral and cubic patterns at $Ra = 2000$, 14000 and 70000. Contouring information is given in table 4(*a*).

tetrahedral pattern do not change shape with depth. However, for $Ra > 35000$, the upwelling regions are approximately triangular at the top and almost clover-shaped at the bottom. This appears to be caused by the break up of the downwelling regions from a network of linear sheets at the top, to a pattern of connected plumes at the bottom. This effect is most striking at $Ra = 70000$ where the break up begins midway through the shell. Since the downwelling sheets do not have uniform intensity, when they impinge on the bottom boundary they do not spread out into the boundary layers uniformly. Hence, the mass flux which the boundary layers feed into the upwelling plumes is not isotropic with respect to the axes of the plumes. In

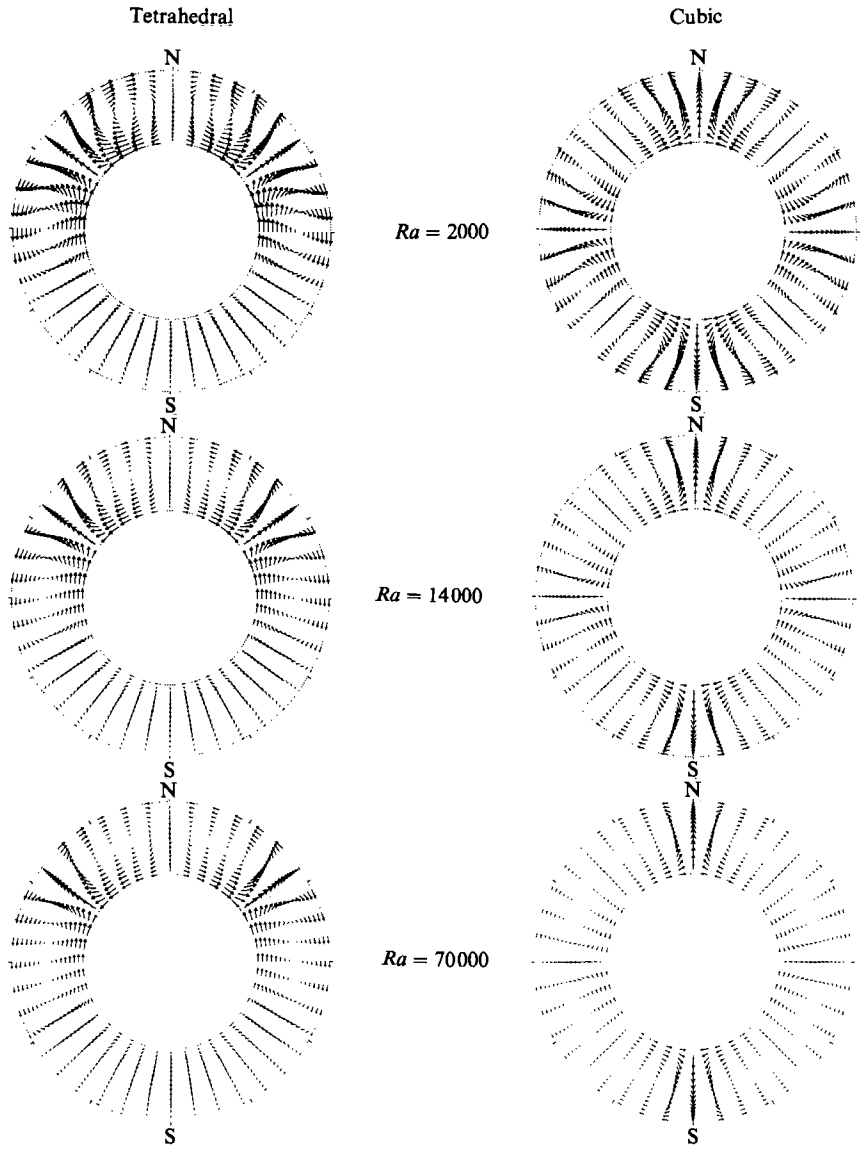

FIGURE 8. Velocity vectors in the constant longitude plane $\phi = 0$ for the convective solutions of figure 6. Vector information is listed in the following table. The magnitudes of the maximum velocity vectors for the tetrahedral solution at $Ra = 2000$, 14000 and 70000 are 26.3, 135.0 and 361.0, respectively. The magnitudes of the maximum velocity vectors for the cubic solution at $Ra = 2000$, 14000 and 70000 are 31.2, 205.0 and 742.0, respectively.

contrast, the upwelling regions impinge on the upper boundary as narrow cylinders (especially at $Ra = 70000$) and are more likely to spread uniformly.

6.2. *Vertical structure of velocity and temperature fields*

Figure 6 shows spherically-averaged temperature profiles for various Ra (for only the tetrahedral pattern since the profiles of the cubic pattern are essentially identical). As Rayleigh number increases, a large central portion of the shell becomes more stably stratified as the boundary layers narrow. Figures 7 and 8 show isotherms and

velocity vectors in a plane of constant longitude for both the tetrahedral and cubic solutions at $Ra = 2000$, 14000 and 70000. The upwelling and downwelling regions narrow as Ra increases. The upwelling regions in general appear more intense than the downwelling ones; however, the cross-sections of constant longitude do not always pass through both the upwelling and downwelling maxima. The isotherm plots at high Ra reveal the delamination of the upper cold boundary layer: fingers of cold fluid sink from the top boundary layer before the layer reaches the major downwelling.

Conservation of energy for steady solutions requires the heat flow across the lower boundary to be $(r_2/r_1)^2$ of that across the upper boundary (since the net heat flux into the shell must equal the net heat flux out). The spherically-averaged profiles of figure 6 show that this constraint is almost completely satisfied by the relative temperature drops across the upper and lower boundary layers: the temperature drop across the bottom thermal boundary layer is approximately $(r_2/r_1)^2$ times the temperature drop across the top thermal boundary layer. Thus, the thermal boundary layers at the top and bottom of the shell have essentially the same thickness (see also Zebib *et al.* 1980). However, given the differences in horizontal velocities (see figure 8) and characteristic horizontal lengths of the boundary layers at the top and bottom boundaries, there is no *a priori* reason to expect the thermal boundary layers to be of equal thickness. One possible explanation for their comparable thicknesses is that such an arrangement minimizes the net amount of gravitationally unstable fluid in the boundary layers. The net amount of unstable mass in the boundary layers is proportional to $M = \Delta T_1 \delta_1 r_1^2 + \Delta T_2 \delta_2 r_2^2$, where ΔT is the temperature drop across the boundary layer, δ is the boundary-layer thickness and the subscripts on ΔT and δ have the same meaning as those on r. Since, by conservation of energy, $\Delta T_1 r_1^2/\delta_1 = \Delta T_2 r_2^2/\delta_2$, then $M = \Delta T_2 r_2^2 \delta_1 (f + 1/f)$, where $f = \delta_2/\delta_1$. The value of f that minimizes M is $f = 1$. Therefore, a temperature field with top and bottom boundary layers of equal thickness creates optimal stability for the fluid layer.

Geometric compression of the flow field is manifest in the vertical velocity structure in two ways. First, the velocity vectors of figure 8 show that the velocity at the bottom of any convection cell is larger than at the top. Secondly, the centres of the cells are shifted slightly towards the top boundary. Both of these effects facilitate the conservation of mass under geometric compression.

7. Heat flow

7.1. *Global characteristics*

Figure 9 shows Nusselt number versus Rayleigh number for the tetrahedral and cubic solutions in the Ra range of this study. Since the solutions for $Ra \leqslant 14000$ have different resolution from those with $Ra \geqslant 14000$, the Nu curves are not necessarily continuous across $Ra = 14000$. The worst error in Nu is between 1% and 2%. The fit of a power-law relationship to the high Ra end of these curves ($Ra > 15Ra_{cr}$) shows that $Nu \sim Ra^{0.263}$ for the tetrahedral solutions and $Nu \sim Ra^{0.280}$ for the cubic solutions. These exponents are about 20% less than predicted by either boundary-layer theory or mean field theory (Turcotte & Schubert 1982; Olson 1981).

The heat flow for the cubic solution surpasses that of the tetrahedral solution for Ra as large as 70000. However, this does not imply that the cubic pattern is preferred over the other. In fact, the spectral content of the tetrahedral pattern (table 3) has significant $l = 4$, $m = 0$ and $l = 4$, $m = 4$ signatures; if the cubic pattern was indeed preferred, these modes would grow at the expense of the $l = 3$, $m = 2$ mode.

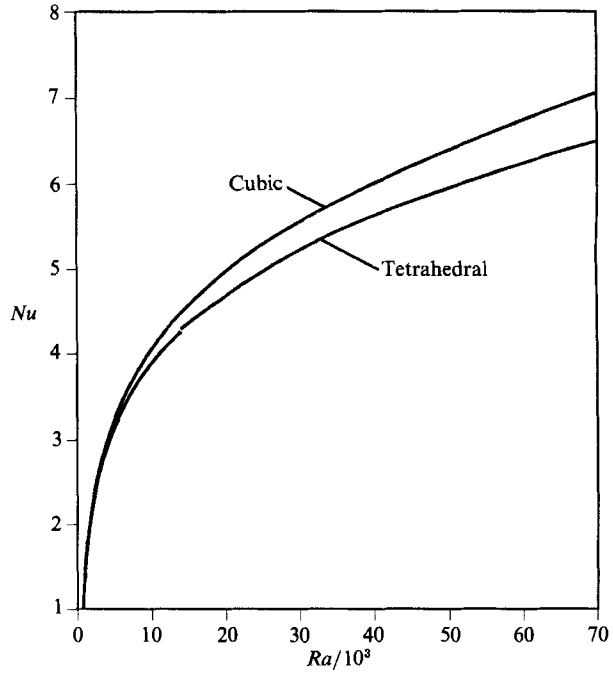

FIGURE 9. Nusselt number Nu versus Rayleigh number Ra for both tetrahedral and cubic patterns. For $712 \leqslant Ra \leqslant 14000$ the truncation levels of the numerical scheme are $L = 21$ and $N = 16$; for $14000 \leqslant Ra \leqslant 70000$ $L = 31$ and $N = 18$.

Similarly, we also found that the cubic solutions are stable against an $l = 3$, $m = 2$ tetrahedral perturbation for several Rayleigh numbers covering the Ra range of this study.

7.2. *Three-dimensional nature*

Figure 10 shows total heat flux contours at the top and bottom of the shell for the tetrahedral and cubic patterns at $Ra = 70000$. The maximum heat flow at a boundary occurs where vertically moving fluid impinges on the boundary (downwellings at the bottom, upwellings at the top) since the fluid increases the temperature contrast at the boundary and compresses the isotherms in the boundary layer; the minimum heat flow at a boundary occurs where fluid moves away from the boundary since the fluid has almost the same temperature as the boundary and its motion stretches the isotherms towards the middle of the shell (see also figure 7). Although the mean heat flux at the bottom is larger than at the top, the maximum heat flux at the top is greater than at the bottom. The maximum heat flux out of the shell over upwelling regions is approximately nine times the mean heat flux at the top for the tetrahedral solution and seven times the mean heat flux for the cubic solution (even though the mean heat flux for the cubic solution is 10% greater than that for the tetrahedral solution). Alternatively, the maximum heat flux into the shell beneath downwelling regions is less than twice the mean heat flow at the bottom for both convective patterns. At the bottom boundary, the minimum heat flux (occurring where fluid moves away from the boundary) is usually one order of magnitude less than the maximum heat flux. At the top boundary, the minimum heat flux is usually two orders of magnitude less than the maximum heat flux and can be negative, which may relate to the entrainment of warm material into the downwelling currents (see §6.1).

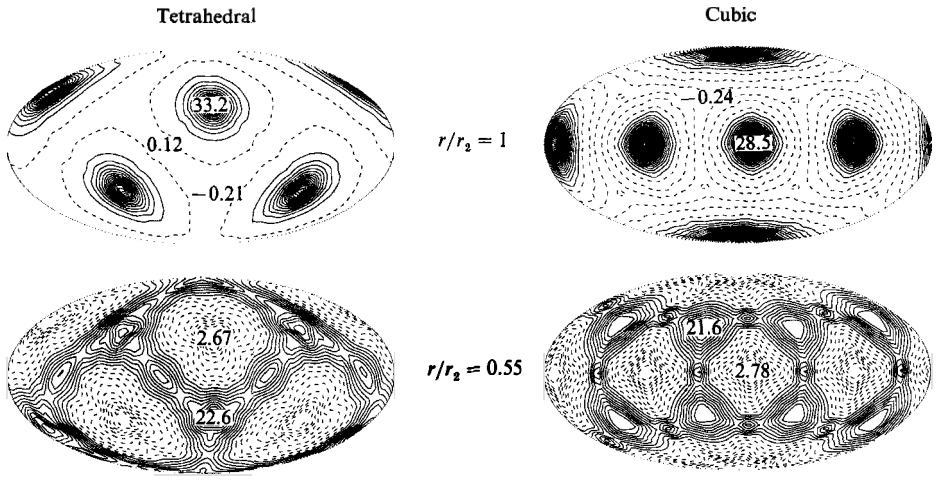

FIGURE 10. Contours of total heat flux for the tetrahedral and cubic patterns at the top ($r/r_2 = 1$) and bottom ($r/r_2 = 0.55$) of the shell at $Ra = 70000$. Dashed lines are for heat fluxes that are less than the mean (spherically-averaged) heat flux, solid lines are for heat fluxes greater than the mean heat flux. Numerical values are maximum and minimum heat fluxes, non-dimensionalized by $k\Delta T/d$. The mean non-dimensional heat flux of the tetrahedral pattern at the top of the shell is 3.61, and at the bottom it is 12.00. The mean heat flux of the cubic pattern at the top is 3.92 and at the bottom it is 13.07. Contouring information is given in table 4(*b*).

8. Stability of patterns to flow reversal

The patterns of convection in spherical shells in the small-amplitude analytic theory of Busse (1975) and Busse & Riahi (1982) are independent of flow direction. This implies that the finite-amplitude convective patterns of this paper might be stable to flow reversal. Stability to flow reversal is well established in three-dimensional convection in a plane layer where upwellings and downwellings are symmetric with respect to the midplane (Busse 1981). However, spherical geometry destroys the midplane symmetry. Accordingly, upwelling and downwelling regions of the tetrahedral and cubic planforms are morphologically distinct. Thus, we attempted to test the existence of reversed solutions for both patterns by changing the sign of the velocity and aspherically symmetric temperature fields of solutions at $Ra = 2000$, 7000 and 14000 and, using them as initial conditions, time integrating the convective equations to steady state.

At $Ra = 2000$ and 7000, the reversed cubic solution temporarily settles into a metastable solution that maintains the cubic signature (the ratio of the two dominant entropy variances is also $\frac{5}{7}$). However, the upwellings are again cylindrical and concentrated at the corners of a cube (making the pattern exactly cubic), while the downwellings are also cylindrical and at the cube's faces (figure 11). The Nusselt numbers of these solutions are 2.28 at $Ra = 2000$ and 3.85 at $Ra = 7000$ (compared to 2.25 and 3.63 for the original cubic solutions at these Ra).

After time integrating these metastable solutions further they become unstable. At $Ra = 2000$, the metastable solution evolves into a steady, purely axisymmetric solution with two dominant modes whose normalized temperature variances are $\langle \Theta^2 \rangle_{l=4} = 1$ and $\langle \Theta^2 \rangle_{l=2} = 0.62$, corresponding to a pattern with four zonal cells in which downwelling occurs at both poles and uniformly along the equator (figure 11). The Nusselt number of this axisymmetric solution is 2.24. This solution is the same

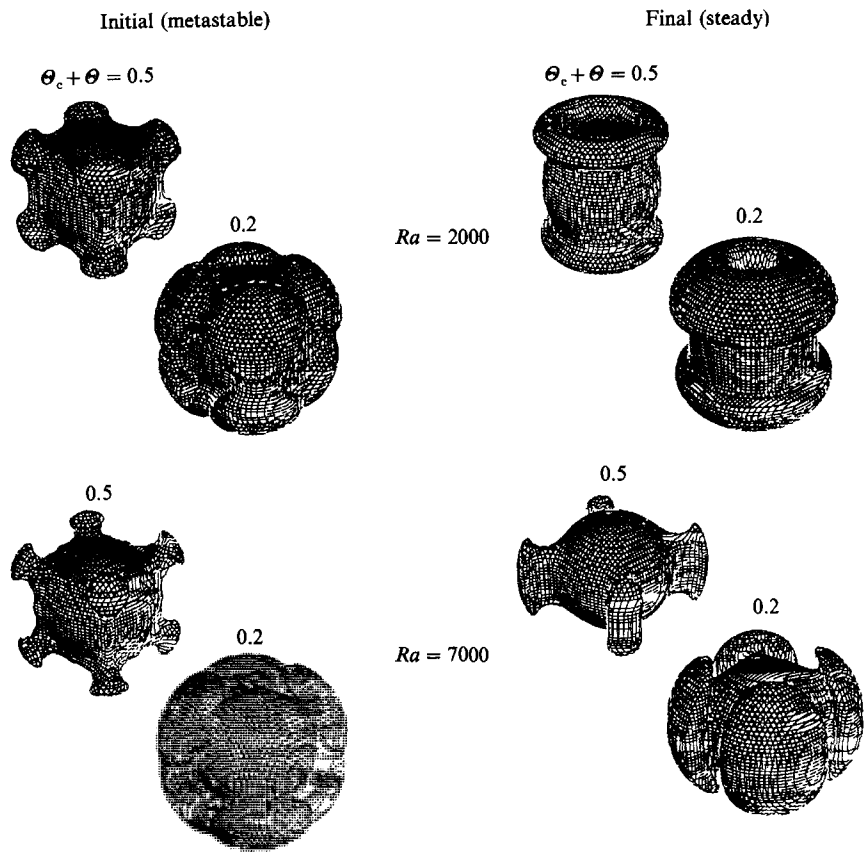

FIGURE 11. Three-dimensional isothermal surfaces of the metastable and final steady solutions obtained after reversal of the cubic solutions for $Ra = 2000$ and 7000. Two surfaces are shown for each case: one for $\Theta_c+\Theta = 0.5$ and the other for $\Theta_c+\Theta = 0.2$.

as the '*el*4' solution found by Bercovici *et al.* (1988). The $Ra = 7000$ metastable solution evolves into a steady tesseral pattern with four elongated cylindrical upwelling regions all on the equator (figure 11); this pattern has two dominant modes with normalized variances $\langle\Theta^2\rangle_{l=4,m=4} = 1$ and $\langle\Theta^2\rangle_{l=2,m=0} = 0.51$ and $Nu = 3.54$. This pattern is similar to the 'M44' pattern found by Machetel *et al.* (1986). At $Ra = 14000$, the reversed cubic solution becomes immediately unstable and evolves into a steady purely axisymmetric, $l = 2$ dominant solution similar to the one used to test the numerical codes in §4; the Nu for this solution is 3.91 while the original non-reversed cubic solution has $Nu = 4.49$.

At $Ra = 2000$ and 7000, the reversed tetrahedral solutions evolve into steady solutions that also have a tetrahedral signature. However, the secondary cubic signature of the tetrahedral pattern has almost vanished and the second largest mode has $l = 6$, $m = 4$. These solutions have four cylinders of downwelling surrounded by a network of upwelling (figure 12) in which the most intense upwelling occurs within cylindrical features located at the apexes of a tetrahedron. The Nu of these two new tetrahedral solutions are 2.29 at $Ra = 2000$ and 3.81 at $Ra = 7000$ (compared to 2.20 and 3.51 for the original tetrahedral pattern at these Ra). At $Ra = 14000$ the reversed tetrahedral solution becomes unstable and returns to the original tetrahedral pattern (with a 90° longitudinal shift). The instability of steady solutions

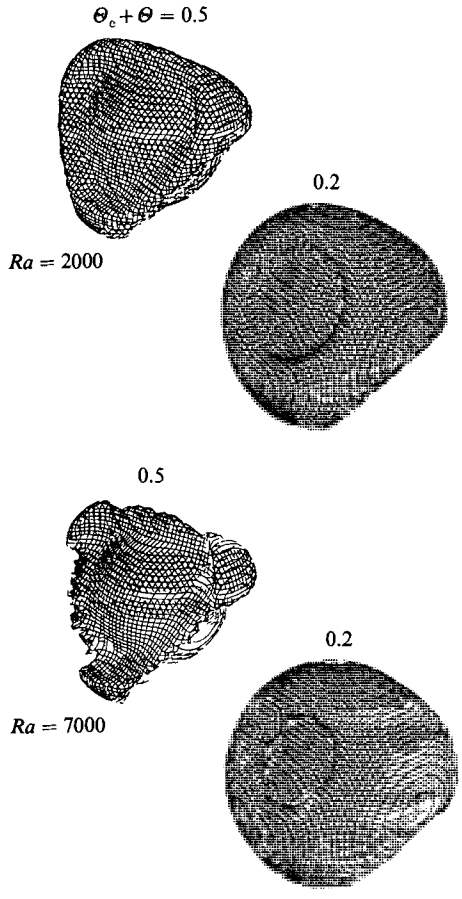

FIGURE 12. Three-dimensional isothermal surfaces of the steady solutions obtained after reversal of the tetrahedral solutions at $Ra = 2000$ and 7000. Two surfaces are shown for each case at the same isotherm values as in figure 11.

to flow reversal was also experienced by Machetel *et al.* (1986) for an $l = 4$, $m = 3$ dominant solution which (upon flow reversal) became an axisymmetric solution. The instability of the reversed tetrahedral solution at $Ra = 14000$ is manifest as the growth of the concentrated upwellings at the expense of the upwelling bridges to form the original tetrahedral pattern.

Small-amplitude analytic theory offers insight into why, at low Ra, the tetrahedral (odd l) pattern is stable to flow reversal while the cubic (even l) pattern is not. In the perturbation analysis of Busse (1975) and Busse & Riahi (1982), the Rayleigh number Ra is expanded in terms of a small amplitude parameter ϵ such that

$$Ra = Ra_{\mathrm{cr}} + \epsilon Ra^{(1)} + \ldots + \epsilon^{(n)} Ra^{(n)} + \ldots.$$

The sign of the solution, hence the flow direction, is determined by the sign of $\epsilon Ra^{(1)}$. When l is odd, $Ra^{(n)}$ is zero for odd n, and the flow direction is degenerate for odd l patterns. As shown in Busse & Riahi (1982), solutions with $\epsilon Ra^{(1)} < 0$ are unstable. Thus, reversing the flow of the stable cubic pattern yielded a metastable solution which might correspond to the unstable solution with negative $\epsilon Ra^{(1)}$ predicted by small-amplitude theory. Since $\epsilon Ra^{(1)}$ is zero for the odd l patterns, the stability of the

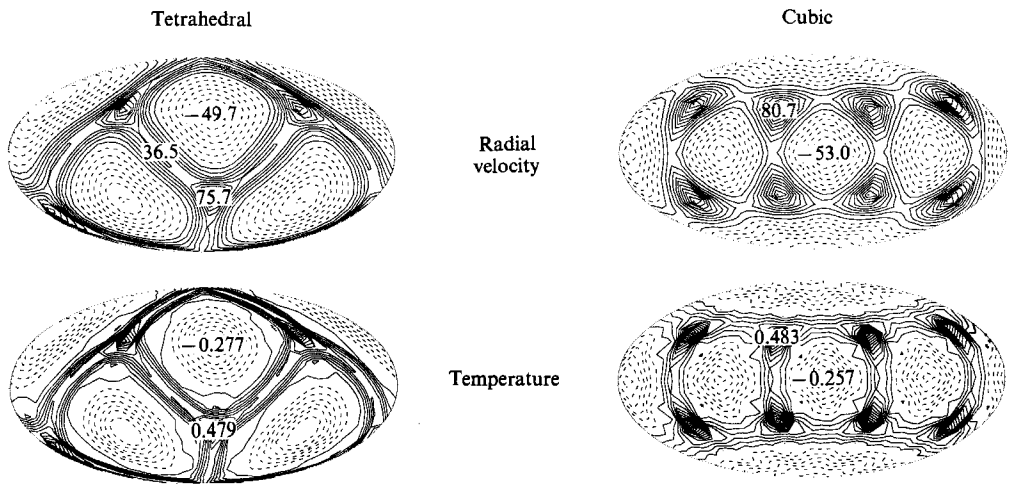

FIGURE 13. Radial velocity contours and isotherms (relative to the spherically-averaged temperature) on a spherical surface midway through the shell for the metastable solution obtained after reversal of the cubic solution and the steady solution found after reversal of the tetrahedral solution at $Ra = 7000$. Labelling of maxima is the same as in figures 3 and 4. Contouring information is given in table 4(*c*).

tetrahedral pattern does not preclude the stability of the reversed tetrahedral pattern. Since the tetrahedral pattern is, in fact, a mixed mode pattern with a minor cubic signature, its reversal may result in the destabilization and elimination of the cubic component and the maintenance of the tetrahedral component.

The metastable cubic solutions obtained after flow reversal at $Ra = 2000$ and 7000, while they exist, have slightly greater Nu than the original cubic solutions, yet when they grow unstable and evolve to truly steady patterns, Nu drops well below that of the original cubic solutions. At $Ra = 14000$ the reversed cubic solution immediately transitions to an axisymmetric pattern with a Nu that is 60% less than that of the original cubic solution at the same Ra. Similarly, the steady tetrahedral solutions obtained after flow reversal are characterized by greater heat flow than the original tetrahedral solutions, yet at $Ra = 14000$ they return to the original tetrahedral pattern.

Finally, the horizontal velocity and temperature structures of the (metastable) cubic and (stable) tetrahedral solutions obtained after flow reversal are not quantitatively the negative of the original cubic and tetrahedral solutions (figure 13). Instead of the maximum velocities and temperature anomalies occurring in the downwelling regions (as they should if the flow is truly reversed), they again occur in the upwelling regions. Therefore, even if a convective pattern is stable (or metastable) to flow reversal, the convective solutions change in detail.

9. Discussion

9.1. *Physical interpretation*

Several results of numerical experiments in thermal convection do not support the assumption that convection acts to maximize heat flow. In previous work, with bifurcations from one steady state to another, Nusselt number is as likely to decrease as increase (e.g. Machetel & Rabinowicz 1985). In this study, neither the cubic nor

tetrahedral pattern is preferred over the other, even though their heat flow characteristics differ. In addition, when the reversed solutions (§8) become unstable, they always transition to solutions characterized by lower Nu.

Alternatively, numerical experiments in convection often indicate a tendency of convective solutions to assume planforms that reduce, or minimize, the viscous shear on upwelling and/or downwelling regions. For example, it has been found that for axisymmetric spherical steady state convection, bifurcations with increasing Ra tend to increase convection cell wavelength; that is, a four- or three-cell structure changes to a two-cell structure (Machetel & Rabinowicz 1985; Bercovici *et al.* 1988). This reduces the shear between upwelling and downwelling regions and the effective surface area of the vertically moving regions upon which the viscous shear acts (e.g. by fusing two upwelling regions into one). A possible reason for this tendency is that given a force balance in an upwelling (or downwelling) region, the reduction of shear causes the upwelling (downwelling) velocity to increase in magnitude in order to maintain the viscous force that balances the buoyancy and pressure forces of the rising (sinking) fluid. The greater upwelling (downwelling) velocity allows for more efficient release of gravitational potential energy. In the above example of bifurcations of axisymmetric steady solutions, it has been found that upon bifurcation with increasing Ra, boundary deflection (along with convection cell wavelength) always increases, which reflects the increase in upwelling and downwelling velocities (Bercovici *et al.* 1988).

In three-dimensional convection with any geometry, a cylindrical upwelling or downwelling will necessarily be surrounded by a sheet-like return flow. The hexagonal pattern of convection in a planar geometry maintains upwellings and downwellings with both sheet-like and cylindrical natures since the pattern is symmetric about the midplane of the fluid layer. For example, upwellings emanate from the bottom boundary as three sheets at 120° to each other and converge into a cylindrical plume at their axis; downwellings simply mirror this behaviour. However, in spherical convection the midplane symmetry is broken and the preferred mode of upwelling is in cylinders and that of downwelling is in linear sheets throughout most of the shell. Although the downwelling regions lose most of their sheet-like signature near the bottom of the shell, as in the plane-layer hexagonal pattern, the upwelling regions are distinctly cylindrical throughout the entire fluid layer. Because the lower boundary layer has a greater temperature drop across it than the upper one, the buoyant density anomalies and hence velocities of upwelling regions will be greater than those of the downwelling regions. Accordingly, the upwelling plumes will, by conservation of mass, have smaller cross-sectional (i.e. horizontal) area than the downwelling regions. Therefore, since the upwelling regions have both a small cross-sectional area and large velocity, they are more sheared than the downwelling regions. The net shear on the upwelling and downwelling regions is minimized by allowing the region with maximum shear (the upwelling region) to assume the shape with minimum effective surface area (a cylinder), while the region with less shear (the downwelling region) assumes the shape with the larger surface area (a two-dimensional sheet). The prominence of upwelling cylinders and downwelling sheets leads to the large vertical velocities that allow for efficient release of gravitational potential energy.

The predominance of upwelling cylinders and downwelling sheets may also be largely determined by the spherical geometry of the fluid layer. When two planar horizontal boundary-layer flows converge, they are eventually forced to bend and move away from the boundary surface in a sheet-like flow. If the boundary-layer

flows are constrained to move on a spherical surface, the sheet-like flow away from the surface will be stretched (compressed) along the plane of the sheet as it moves radially outwards (inwards) from the spherical surface; radial outward (inward) motion corresponds to upwelling (downwelling) in the spherical shell. Hence, a downwelling sheet tends to thicken and become concentrated as it descends. An upwelling sheet would become stretched and dispersed. Downwelling motion in a spherical geometry therefore tends to preserve sheet-like structures, while upwelling motion tends to disrupt them. The cylindrical shape of upwelling plumes may then occur because once the sheet-like structure disintegrates, the flow coalesces into shapes with minimum surface area to reduce the net viscous shear opposing their motion. In plane-layer convection with temperature-dependent viscosity, the least viscous region (hot upwelling in a liquid, cold downwelling in a gas) always occurs along the plume-like axis of a hexagonal convection cell (Busse 1978). Thus, the narrowest, most sheared region of flow may form in a way that best reduces viscous resistance.

9.2. *Geophysical interpretation*

The tendency of downwelling regions to be in the form of two-dimensional sheets in three-dimensional spherical convection is geophysically significant since that is the mode of downwelling in the Earth's mantle. Descending slabs represent the fundamental mode of downwelling in spherical convection; it is not necessary to appeal to considerations of temperature dependence of rheology to explain the sheet-like character of cold downwellings in the Earth's mantle (although this rheological behaviour obviously enhances the integrity of the slabs). The break up of downwelling sheets may also have a bearing on the fate of cold subducting slabs as they sink into the mantle. Measurements of seismic velocity anomalies around subducted slabs indicate that descending slabs penetrate well into the lower mantle (Creager & Jordan 1984). In addition, measurements of core-mantle boundary topography show a downward deflection of the boundary beneath subduction zones, implying that slabs at least influence downwelling currents to the very base of the mantle, if they do not reach the core-mantle boundary itself (Creager & Jordan 1986; see review by Silver *et al.* 1988). However, there is still uncertainty about the existence of a well-defined slab signature in the deep lower mantle. This is often attributed to the retardation of slab descent by a stabilizing compositional density increase or a viscosity increase (associated with phase or compositional changes) at the upper mantle–lower mantle interface. However, this study indicates that simple dynamical considerations can account for the break-up of downwelling sheets into broader, more cylindrical features. Therefore, if basal heating at the core–mantle boundary is significant (as implied by recent high-pressure experiments on the melting temperature of iron; Williams *et al.* 1987), then descending slabs may undergo natural disruption, accounting for the apparent absence of a well-defined slab signature in the deep mantle. Cold material still reaches the lower boundary yet the sheet-like downwellings begin to disintegrate halfway through the shell. While a temperature-dependent rheology would probably delay such a slab break-up, a viscosity increase (continuous or discontinuous) with depth in the mantle might cause disintegration to occur even further from the lower boundary. The presence of internal heating would also affect slab break up; for example, a purely heated from within convecting layer has no lower boundary layer into which a downwelling region must diverge.

The geophysical implications of our numerical experiments are limited by (i) the Rayleigh number being at least an order of magnitude less than the Earth's, (ii) the

simple Newtonian rheology of our experiments, and (iii) evidence that internal heating is significant (if not predominant) in the Earth's mantle while it is not included in this study.

The authors wish to acknowledge the helpful comments of two anonymous reviewers. This research was supported by NASA through grant NAG5152, by the University of California, Institute of Geophysics and Planetary Physics, Los Alamos, and by the San Diego Supercomputer Center. All computations and graphics were generated on a Cray XMP-48 at the San Diego Supercomputer Center.

REFERENCES

Ali-Kahn, M. A. 1982 Three-dimensional thermal convection of an infinite Prandtl number fluid in a spherical shell. Dissertation, Rutgers University, The State University of New Jersey.

Baumgardner, J. R. 1985 Three-dimensional treatment of convective flow in the Earth's mantle. *J. Stat. Phys.* **39**, 501–511.

Bercovici, D., Schubert, G. & Zebib, A. 1988 Geoid and topography for infinite infinite Prandtl number convection in a spherical shell. *J. Geophys. Res.* **93**, 6430–6436.

Bloxham, J. & Gubbins, D. 1985 The secular variation of the Earth's magnetic field. *Nature* **317**, 777–781.

Bowin, C. 1986 Topography at the core-mantle boundary. *Geophys. Res. Lett.* **13**, 1513–1516.

Busse, F. H. 1975 Patterns of convection in spherical shells. *J. Fluid Mech.* **72**, 67–85.

Busse, F. H. 1978 Non-linear properties of thermal convection. *Rep. Prog. Phys.* **41**, 1929–1967.

Busse, F. H. 1981 Transition to turbulence in Rayleigh–Bénard convection. In *Hydrodynamic Instabilities and the Transition to Turbulence* (ed. H. L. Swinney & J. P. Gollub). Springer.

Busse, F. H. 1983 Quadrupole convection in the lower mantle? *Geophys. Res. Lett.* **10**, 285–288.

Busse, F. H. & Riahi, N. 1982 Patterns of convection in spherical shells. Part 2. *J. Fluid Mech.* **123**, 283–301.

Busse, F. H. & Riahi, N. 1988 Mixed-mode patterns of bifurcations from spherically symmetric basic states. *Nonlinearity* **1**, 379–388.

Chandrasekhar, S. 1961 *Hydrodynamic and Hydromagnetic Stability*. Clarendon.

Creager, K. C. & Jordan, T. H. 1984 Slab penetration into the lower mantle. *J. Geophys. Res.* **89**, 3031–3049.

Creager, K. C. & Jordan, T. H. 1986 Aspherical structure of the core-mantle boundary from PKP travel times. *Geophys. Res. Lett.* **13**, 1497–1500.

Dziewonski, A. M. 1984 Mapping the lower mantle: Determination of lateral heterogeneity in P velocity up to degree and order 6. *J. Geophys. Res.* **89**, 5929–5952.

Dziewonski, A. M. & Woodhouse, J. H. 1987 Global images of the Earth's interior. *Science* **236**, 37–48.

Glatzmaier, G. A. 1984 Numerical simulations of stellar convective dynamos I. The model and method. *J. Comp. Phys.* **55**, 461–484.

Glatzmaier, G. A. 1988 Numerical simulations of mantle convection: time-dependent, three-dimensional, compressible, spherical shell. *Geophys. Astrophys. Fluid Dyn.* **43**, 223–264.

Gubbins, D. & Richards, M. 1986 Coupling of the core dynamo and mantle: thermal or topographic? *Geophys. Res. Lett.* **13**, 1521–1524.

Hart, J. E., Glatzmaier, G. A. & Toomre, J. 1986 Space laboratory and numerical simulations of thermal convection in a rotating hemi-spherical shell with radial gravity. *J. Fluid Mech.* **173**, 519–544.

Hsui, A. T., Turcotte, D. L. & Torrance, K. E. 1972 Finite amplitude thermal convection within a self-gravitating fluid sphere. *Geophys. Fluid Dyn.* **3**, 35–44.

Machetel, P. & Rabinowicz, M. 1985 Transitions to a two mode axisymmetrical spherical convection: Application to the Earth's mantle. *Geophys. Res. Lett.* **12**, 227–230.

MACHETEL, P., RABINOWICZ, M. & BERNADET, P. 1986 Three-dimensional convection in spherical shells. *Geophys. Astrophys. Fluid Dyn.* **37**, 57–84.

MACHETEL, P. & YUEN, D. A. 1986 The onset of time dependent convection in spherical shells as a clue to chaotic convection in the Earth's mantle. *Geophys. Res. Lett.* **13**, 1470–1473.

MACHETEL, P. & YUEN, D. A. 1987 Chaotic axisymmetrical spherical convection and large-scale mantle circulation. *Earth Planet. Sci. Lett.* **86**, 93–104.

MACHETEL, P. & YUEN, D. A. 1988 Infinite Prandtl number convection in spherical shells. In *Mathematical Geophysics* (eds N. J. Vlaar, G. Nolet, M. J. R. Wortel & S. A. P. L. Cloetingh), Reidel.

MORELLI, A. & DZIEWONSKI, A. M. 1987 Topography of the core-mantle boundary and lateral homogeneity of the liquid core. *Nature* **325**, 678–683.

OLSON, P. 1981 Mantle convection with spherical effects. *J. Geophys. Res.* **86**, 4881–4890.

OLSON, P., SCHUBERT, G. & ANDERSON, C. 1987 Plume formation in the D″-layer and the roughness of the core-mantle boundary. *Nature* **327**, 409–413.

OXBURGH, E. R. & TURCOTTE, D. L. 1978 Mechanisms of continental drift. *Rep. Prog. Phys.* **41**, 1249–1312.

ROBERTS, P. H. 1987 Convection in spherical systems. In *Irreversible Phenomena and Dynamical Systems Analysis in Geosciences* (ed. C. Nicolis & G. Nicolis). Reidel.

SCHUBERT, G., STEVENSON, D. & CASSEN, P. 1980 Whole planet cooling and the radiogenic heat source contents of the Earth and moon. *J. Geophys. Res.* **85**, 2531–2538.

SCHUBERT, G. & ZEBIB, A. 1980 Thermal convection of an internally heated infinite Prandtl number fluid in a spherical shell. *Geophys. Astrophys. Fluid Dyn.* **15**, 65–90.

SILVER, P. G., CARLSON, R. W. & OLSON, P. 1988 Deep slabs, geochemical heterogeneity, and the large-scale structure of mantle convection: investigation of an enduring paradox. *Ann. Rev. Earth Planet. Sci.* **16**, 477–541.

STACEY, F. D. 1977 *Physics of the Earth*. Wiley.

TURCOTTE, D. L. & SCHUBERT, G. 1982 *Geodynamics*. Wiley.

WILLIAMS, Q., JEANLOZ, R., BASS, J., SVENDSON, B. & AHRENS, T. J. 1987 The melting curve of iron to 250 Gigapascals: A constraint on the temperature at the Earth's center. *Science* **236**, 181–182.

WOODHOUSE, J. H. & DZIEWONSKI, A. M. 1984 Mapping the upper mantle: Three dimensional modeling of earth structure by inversion of seismic wave-forms. *J. Geophys. Res.* **89**, 5953–5986.

YOUNG, R. E. 1974 Finite-amplitude thermal convection in a spherical shell. *J. Fluid Mech.* **63**, 695–721.

ZEBIB, A., SCHUBERT, G. & STRAUS, J. M. 1980 Infinite Prandtl number thermal convection in a spherical shell. *J. Fluid Mech.* **97**, 257–277.

ZEBIB, A., SCHUBERT, G., DEIN, J. L. & PALIWAL, R. C. 1983 Character and stability of axisymmetric thermal convection in spheres and spherical shells. *Geophys. Astrophys. Fluid Dyn.* **23**, 1–42.

ZEBIB, A., GOYAL, A. K. & SCHUBERT, G. 1985 Convective motions in a spherical shell. *J. Fluid Mech.* **152**, 39–48.